CHEMISTRY OF MATERIALS

pubs.acs.org/cm Article

Tunable Salt-Inclusion Chalcogenides for Ion Exchange, Photoluminescence, and Scintillation

Anna A. Berseneva, Lakshani W. Masachchi, Luiz G. Jacobsohn, and Hans-Conrad zur Loye*

Cite This: Chem. Mater. 2023, 35, 1417−1431

Read Online

ACCESS | Metrics & More | Article Recommendations | Supporting Information

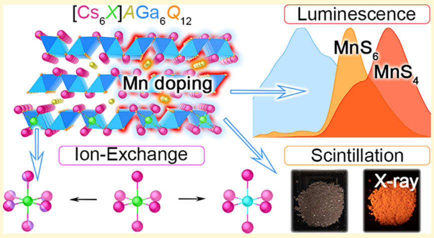

ABSTRACT: Salt-inclusion chalcogenides (SICs) consisting of covalent and ionic building blocks have emerged as functional materials exhibiting novel topologies that result from the combination of the chalcogenide-based frameworks and the salt inclusions contained within them. Nine compositions of a novel family of SICs $[Cs_6X]AGa_6Q_{12}$ (A = Na, K, and Rb; X = F, Cl, and Br; Q = S and Se) were synthesized *via* halide/polychalcogenide flux crystal growth and structurally characterized. *Ex situ* powder X-ray diffraction analysis was used to determine the optimal synthesis temperatures at which the titled SIC materials crystallized in the flux. Density functional theory calculations coupled with convex hull construction were performed to predict the stability of $[Cs_6X]AGa_6Q_{12}$ compositions as a function of X, A, and Q and to identify their decomposition pathways. A combination of single-crystal X-ray diffraction and energy-dispersive spectroscopy was used to study single-crystal-to-single-crystal (SC-SC) ion-exchange-reaction, a process that also allowed for the synthesis of two additional members of this family, $[Cs_6F]NaGa_6S_{12}$ and $[Cs_{6-x}Rb_xBr]RbGa_6S_{12}$, which did not form during the direct flux crystal growth. Furthermore, single crystals of $[Cs_6X]AGa_6Q_{12}{:}Mn^{2+}$ were obtained through direct flux crystal growth and SC-SC ion-exchange reactions and studied for their photoluminescent behavior using individual single crystals. The emission profile changed as a function of Mn^{2+}-content, the A cation identity, and the synthesis method used. Finally, radioluminescence measurements were carried out on $[Cs_6Cl]NaGa_6S_{12}{:}Mn^{2+}$ bulk samples, resulting in bright orange scintillation.

INTRODUCTION

Advances in synthetic chalcogenide chemistry have accelerated the discovery of functional materials as well as stimulated the development of numerous technological applications for these materials, all helped by an increased understanding of composition−property relationships.[1,2] Chalcogenide-based compounds occupy a unique position in material chemistry due to the soft nature of the chalcogen elements and emerging covalent metal chalcogenide bonding, which results in a rich and diverse crystal chemistry.[1,3] In fact, the electronic structure of chalcogenide materials favors their applications as quantum materials, catalysts, ion-exchange materials, ion-conductors, luminophores, thermoelectric materials, and semiconductors.[4−20] Recent advances in developing convenient synthetic approaches have enabled the rational synthesis of new functional chalcogenide-based materials containing a wide range of elements, resulting in various material types, ranging from nanoparticles to large single crystals of pure inorganic compositions and hybrid structures.[21−45] Another new material type that has emerged from these investigations is salt-inclusion chalcogenide materials (SICs)[46,47] that exhibit novel framework topologies and possess ionic inserts (salt-inclusions).

SICs are an emerging class of materials consisting of a covalently bonded framework containing a salt moiety, typically a halogenide (X) coordinated by alkali and alkaline-earth cations (A). In other words, SIC structures can be described as porous frameworks constructed from covalent, metal-centered polyhedral building blocks, MQ_n, that accommodate anion-centered polyhedra, XA_m, in the framework cavities.[46−48] Due to the spatial separation of the covalent framework and the ionic salt-inclusion, SICs exhibit excellent non-linear optical (NLO) properties and ultralow thermal conductivities.[46,49−64] In some cases, the salt-inclusion and the framework maintain both their structural and electronic identity,[65−67] creating low-dimensional forms of known functional materials that find applications in low-dimensional anisotropic magnetic materials, transparent semiconductors, and superconductors.[66,68−73]

A recent review of SICs by Lin et al.[46] highlighted that the asymmetric GaQ_4 polyhedron is one of the most common building blocks for SICs, where a typical GaQ_4-based SIC framework consists of GaQ_4, pseudo-T_2 Ga_4Q_{10} or MGa_3Q_{10} supertetrahedral units. The related Ga_3Q_9 building block is less common, and only a few examples of it have been reported to date, including $[LiCs_2Cl]LiGa_3S_6$,[49] $[Cs_6Cl]_6Cs_3Ga_{53}Se_{96}$,[74] and $[Cs_6Cl]GeGa_5Q_{12}$ (Q = S and Se, Figure S1).[75] The exploration of new GaQ_4-based SIC materials is of interest to

Received: December 1, 2022
Revised: January 6, 2023
Published: January 23, 2023

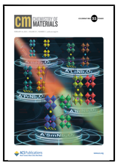

https://doi.org/10.1021/acs.chemmater.2c03592
Chem. Mater. 2023, 35, 1417−1431

better understand the stabilization principles of non-typical GaQ_4 arrangements, such as those of Ga_3Q_9 units. Consequently, developing new salt-inclusion materials is an essential step toward expanding the SIC materials library with compositions that can exhibit desirable properties. One potential application of chalcogenide-based frameworks is as optical materials, where covalently bound moieties act as a host for luminophore impurities. Integration of luminescent centers into novel topologies of covalent and ionic building blocks in SIC materials represents a potential synthetic route to luminescing and scintillating materials. However, limited research efforts have been directed toward exploring SICs' optical properties.[54,56,57,75]

Herein, we demonstrate the versatility of SIC structural families by describing 11 members of a new structure type, $[Cs_6X]AGa_6Q_{12}$ (Figure 1), (A = Na, K, and Rb; X = F, Cl, and Br; Q = S and Se): $[Cs_6F]NaGa_6S_{12}$, $[Cs_6Cl]NaGa_6S_{12}$, $[Cs_{6-x}Na_xBr]NaGa_6S_{12}$, $[Cs_{6-x}K_xCl]KGa_6S_{12}$, $[Cs_{6-x}K_xBr]KGa_6S_{12}$, $[Cs_{6-x}Rb_xCl]RbGa_6S_{12}$, $[Cs_{6-x}Rb_xBr]RbGa_6S_{12}$, $[Cs_6Cl]NaGa_6Se_{12}$, $[Cs_6Br]NaGa_6Se_{12}$, $[Cs_{6-x}K_x Cl]KGa_6Se_{12}$, and $[Cs_{6-x}K_xBr]KGa_6Se_{12}$. We applied density functional theory (DFT) calculations for a fast stability screening of the $[Cs_6X]AGa_6Q_{12}$ series as a function of A, X, and Q. Since $[Cs_{6-x}A_xX]AGa_6Q_{12}$ are kinetic products and have a limited temperature range within which they can be synthesized, we utilized ion-exchange reactions to form kinetically trapped $[Cs_6F]NaGa_6S_{12}$ and $[Cs_{6-x}Rb_xBr]RbGa_6S_{12}$ phases, which could not be obtained using direct synthetic routes. Based on these synthetic strategies, we also successfully utilized $[Cs_6X]AGa_6Q_{12}$ as a host framework for Mn doping to induce photoluminescent and scintillating behavior reported herein.

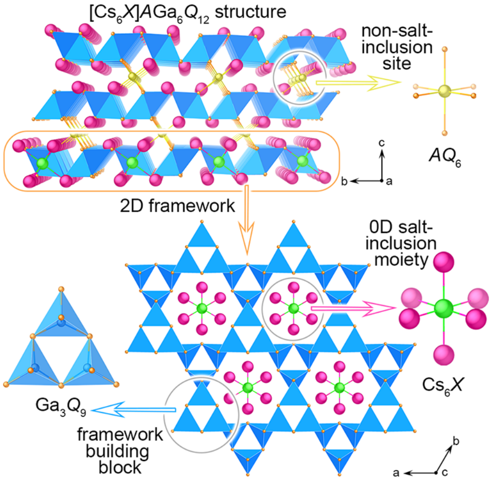

Figure 1. (*top*) View of the $[Cs_6X]AGa_6Q_{12}$ structure highlighting (*bottom*) the dimensionalities of the building blocks. Pink, green, yellow, and orange spheres and blue tetrahedra represent Cs, X, A, and Q atoms and GaQ_4 polyhedra, respectively.

■ EXPERIMENTAL SECTION

Physical Measurements. *Single-Crystal X-ray Diffraction (SCXRD).* SCXRD data were collected at 299(2)−302(2) K on a Bruker D8 QUEST diffractometer equipped with an Incoatec IμS 3.0 microfocus radiation source (MoKα, λ = 0.71073 Å) and a PHOTON II area detector. The crystals were mounted on a microloop using immersion oil. The raw data reduction and absorption corrections were performed using SAINT and SADABS programs.[76,77] Initial structure solutions were obtained with SHELXS-2017 using direct methods and Olex2 GUI.[78] Full-matrix least-square refinements against $|F|^2$ were performed with SHELXL software.[79] The crystallographic data and results of the diffraction experiments are summarized in Tables S1−S7.

Powder X-ray Diffraction (PXRD). PXRD data were collected on a Bruker D2 PHASER diffractometer using Cu Kα radiation (λ = 1.5418 Å) over the 2θ range 5−65° with a step size of 0.02° for 30 min.

Energy-Dispersive Spectroscopy (EDS). EDS was performed directly on crystals mounted on an SEM stub with carbon tape. Quantitative elemental analysis was carried out using a Tescan Vega-3 SEM instrument equipped with a Thermo EDS attachment. The SEM was operated in the low-vacuum mode with a 30 kV accelerating voltage and a 120 s accumulating time. The EDS results are summarized in Table S8 and Figures S2−S13.

Differential Scanning Calorimetry (DSC) and Thermogravimetric Analysis (TGA). DSC/TGA were performed on polycrystalline powder samples using a SDT Q600 Thermogravimetric Analyzer. An alumina pan was used as the sample holder. Samples were heated from room temperature to the target temperature (700 °C or 900 °C) at 10 °C/min under a flow of nitrogen gas (100 mL/min), and the resulting powders were analyzed by PXRD for phase identification.

Inductively Coupled Plasma Mass Spectrometry (ICP-MS). Each sample was digested with 4 mL of aqua regia at 180 °C for 5 h. The resulting solution was diluted to 5 mL and analyzed using a Finnigan ELEMENT XR double-focusing magnetic sector field inductively coupled plasma-mass spectrometer (SF-ICP-MS). A 0.2 mL/min Micromist U-series nebulizer (GE, Australia), quartz torch, and injector (Thermo Fisher Scientific, USA) were used for sample injection.

UV−Visible (UV−vis) Spectroscopy. UV−vis spectra were recorded using a Perkin-Elmer lambda 35 scanning spectrophotometer. The spectrophotometer was operated in diffuse reflectance mode and equipped with an integrating sphere. Reflectance data were converted internally to absorbance *via* the Kubelka−Munk function. Spectra were recorded in the 200−900 nm range.

Photoluminescence. Microphotoluminescence data were collected on a HORIBA Scientific Standard Microscope Spectroscopy System equipped with a Horiba iHR320 imaging spectrograph and a Syncerity CCD detector. A confocal 375 nm diode laser was used as an excitation source. Data were collected using Labspec 6 in the 400−800 nm range with a laser excitation source power of 10.0 mW and a 10× UV objective.

Scintillation. Scintillation images of single crystals were taken using a digital camera inside a Rigaku (Tokyo, Japan) Ultima IV diffractometer equipped with a Cu Kα source (λ = 1.54018 Å). Radioluminescence measurements were collected on a customer-designed configuration of the Freiberg Instruments Lexsyg Research spectrofluorometer equipped with a Varian Medical Systems VF-50J X-ray tube with a tungsten anode. The X-ray source was coupled with an ionization chamber for continuous radiation intensity monitoring. The light emitted by the sample was collected by an Andor Technology SR-OPT-8024 optical fiber connected to an Andor Technology Shamrock 163 spectrograph coupled to a cooled (−80 °C) Andor Technology DU920P-BU Newton CCD camera (spectral resolution of ~0.5 nm/pixel). Powders filled ~8 mm diameter, 0.5 mm deep cups, thus allowing for relative radioluminescence intensity comparison between different samples. Bismuth germanium oxide (BGO) powder [Alfa Aesar Puratronic, 99.9995% (metal basis)] was used as a reference. Radioluminescence was measured under continuous X-ray irradiation (40 kV, 1 mA) with an integration time of 5 s. Spectra were automatically corrected using the spectral response of the system determined by the manufacturer. Radioluminescence measurements as a function of temperature were executed under continuous heating with a 0.5 °C /s heating rate and a 5 s integration time. Thus, the temperature increased by 2.5 °C during the acquisition of each spectrum. Spectra were labeled by the starting temperature.

Computational Details. All DFT calculations were carried out using the Vienna ab initio simulation package (VASP)[80,81] utilizing the projector augmented-wave (PAW) potential.[82] The PBE parametrization of the generalized gradient approximation (GGA) to the exchange-correlation functional was used for the calculations.[83] We used the following potentials of the constituent elements: Li_sv ($1s^2$ $2s^1$), F ($2s^2$

$2p^5$), Na_pv ($2p^6$ $3s^1$), S ($3s^2$ $3p^4$), Cl ($3s^2$ $3p^5$), K_sv ($3s^2$ $3p^6$ $4s^1$), Ga ($3s^2$ $3p^1$), Se ($4s^2$ $4p^4$), Br ($4s^2$ $4p^5$), Rb_sv ($4s^2$ $4p^6$ $5s^1$), I ($5s^2$ $5p^5$), and Cs_sv ($5s^2$ $5p^6$ $6s^1$). All compounds were structurally relaxed (volume, cell shape, and atomic positions) starting from their experimentally known crystal structures, where available, following the DFT settings in the open quantum materials database (OQMD).[84,85] The threshold for energy convergence was set to 10^{-6} eV. The relaxed geometries of the $[Cs_6X]AGa_6Q_{12}$ compounds preserve the $R-3m$ space group during structure relaxation. The energy cutoff for the DFT calculations was set to 520 eV for static calculations. The optimized lattice constants agree very well (error < 3%) with the experimental values.

In relation to the current experimental work, we assessed the $T = 0$ K thermodynamic stabilities of the $[Cs_6X]AGa_6Q_{12}$ compounds. We calculated their formation energies, $\Delta H_f^{0K} = E(\sigma) - \sum_i n_i\mu_i$, where E is the DFT-calculated total energy at 0 K for a compound σ, n_i is the fraction of the ith element with chemical potential μ_i. Utilizing the formation energies of these compositions and all other compounds that are present in each quaternary or penternary phase space, we constructed the quaternary/penternary convex hull for $[Cs_6X]AGa_6Q_{12}$ in the OQMD that allowed us to estimate decomposition energies. Typical decomposition of $[Cs_6X]AGa_6Q_{12}$ leads to either AX and $CsGaQ_2$ or CsX, $CsGaQ_2$, and $AGaQ_2$ (Reactions 1 and 2). All decomposition enthalpies are negative, indicating that these compounds are not thermodynamically stable at 0 K.

Synthesis. *Materials.* The following materials were used as received without further purification: S (Fisher Scientific, 99%), Mn (CERAC, 99.95%), Ga (BTC, 99.999%), Se (Alfa Aesar, 99.999%), Na_2S (Alfa Aesar, 95%), $MnCl_2$ (Acros Organics, 99%), NaF (Alfa Aesar, 99%), CsF (Thermo Scientific, 99%), CsCl (VWR Chemicals, 99.9%), RbBr (Alfa Aesar, 99.8%), CsBr (Alfa Aesar, 99%), CsI (STREM Chemicals, 99%), Na_2CO_3 (Fisher Scientific, 99%), K_2CO_3 (BDH, 99.0%), Rb_2CO_3 (Alfa Aesar, 99%), Cs_2CO_3 (BTC, 99.9%), and acetone (BDH, 99.5%). A_2CO_3 (A = K, Rb, and Cs) were stored at 260 °C in a drying oven. Synthesis of Na_2Se and K_2S was performed using a reported procedure.[86] For all mentioned reactions, masses of the reagents were mixed inside a silica tube except for the synthesis of $[Cs_6F]NaGa_6S_{12}$ described later. Typically, the silica tube was flame sealed under a vacuum of $<10^{-4}$ Torr. In the case of using carbonates as starting reagents, the tube was placed in a metal spring for containment should the tube burst due to carbon dioxide pressure buildup. The sealed tube was placed vertically into a programmable box furnace with the corresponding temperature profile. Once at room temperature, the tube was cut open and placed into a beaker filled with deionized(DI) water.

$[Cs_{6-x}A_xX]AGa_6Q_{12}$ (A, X, Q = Na, Cl, S; K, Cl, S; Rb, Cl, S; Na, Br, S; K, Br, S; Na, Cl, Se; K, Cl, Se; and Na, Br, Se). The starting reagents, Ga (0.0540 g), Q, A_2Q, or A_2CO_3 in a 1:2:1 molar ratio, and the eutectic CsX/CsI mixture (~1 g) were used to grow single crystals of $[Cs_{6-x}A_xX]AGa_6Q_{12}$. The furnace with the tube was ramped up to 650 °C in 5 h, held at this temperature for 24 h, and then cooled to 250 °C at a cooling rate of 5 °C/h. After the reaction and work up in water were complete, the final product was filtered and washed with deionized (DI) water and acetone. Single crystals of $[Cs_{6-x}A_xX]AGa_6Q_{12}$ were placed in immersion oil and mounted for SCXRD. The PXRD patterns for the bulk samples match the simulated pattern obtained from SCXRD (Figures S15−S19 and S21−S23). $[Cs_6Cl]NaGa_6S_{12}$ was initially isolated from a reaction that used only a CsCl flux. However, the final product also contained a Ga_2S_3 impurity. The formation of Ga_2S_3 can be avoided if a eutectic CsCl/CsI mixture is used, presumably due to the soft iodide ligand affecting the solubility of Ga_2S_3.[87] The use of Ga metal is essential for promoting the formation of the targeted SIC materials. Otherwise, if $GaCl_3$ was used in the reaction instead of Ga as a starting reagent, the final product consisted of Ga_2S_3 and S_8 crystals. Under the mild reaction conditions of 650 °C, Ga_2S_3, once formed, does not react further.

$[Cs_6F]NaGa_6S_{12}$. The starting reagents, $[Cs_6Cl]NaGa_6S_{12}$ (0.025 g) and CsF (0.055 g)/CsI (0.095 g) flux, were used in the ion-exchange reaction to obtain single crystals of $[Cs_6F]NaGa_6S_{12}$. All solids were placed in the silver tube, which later was crimped and sealed inside a carbon-coated silica tube. The furnace containing the tube was ramped up to 600 °C for 3 h and held at this temperature for 12 h, and then the furnace was turned off. After the reaction and work up in water were complete, the final product was filtered and washed with DI water and acetone. Single crystals of $[Cs_6F]NaGa_6S_{12}$ were placed in immersion oil and mounted for SCXRD. The PXRD pattern for the bulk sample matches the simulated pattern obtained from SCXRD (Figure S14). Previously, we had attempted to use a NaF/CsF flux for the synthesis of fluoride-based salt-inclusion materials starting from the chlorides. The $[Cs_6Cl]NaGa_6S_{12}$ single crystals were placed in a carbon crucible or crimped silver tube and then sealed inside a carbon-coated silica tube or placed into a flow through furnace under N_2 flow. Those trials were unsuccessful due to the high fluidity of the NaF/CsF flux, which readily overflows the crucible and corrodes the silica tube. Those findings are in line with the literature. Wu and coworkers attempted to carry out the anion exchange of Cl^- to F^- in $[Cs_6Cl]_2Cs_5Ga_{15}Ge_9Se_{48}$ using a KF/CsF mixture at 630 °C for 60 h of dwelling time; however, the tube was corroded, and no crystals were found.[88] Therefore, we believe that a significant reduction of F^- concentration in the flux by adding CsI to CsF salt and using the crimped silver tube guided the successful exchange reaction.

$[Cs_{6-x}Rb_xBr]RbGa_6S_{12}$. The starting reagents, $[Cs_{6-x}Rb_xCl]RbGa_6S_{12}$ single crystals (0.025 g) and RbBr (0.047 g)/CsBr (0.103 g) flux, were used in an ion-exchange reaction to obtain single crystals of $[Cs_{6-x}Rb_xBr]RbGa_6S_{12}$. The furnace containing the tube was ramped up to 700 °C for 3 h and held at this temperature for 12 h, and then the furnace was turned off. After the reaction and work up in water were complete, the final product was filtered and washed with DI water and acetone. Single crystals of $[Cs_{6-x}Rb_xBr]RbGa_6S_{12}$ were placed in immersion oil and mounted for SCXRD. The PXRD pattern for the bulk sample matches the simulated pattern obtained from SCXRD (Figure S20). As expected, $[Cs_{6-x}Rb_xBr]RbGa_6S_{12}$ is a kinetic phase, and hence careful control is necessary for ion-exchange reactions, for instance, prolonged heating (24 h vs 12 h) in a CsBr/RbBr flux leads to the decomposition of $[Cs_{6-x}Rb_xBr]RbGa_6S_{12}$ to $CsGaS_2$.

$[Cs_{6-x}Rb_xBr]NaGa_6Se_{12}$. The starting reagents, $[Cs_6Br]NaGa_6Se_{12}$ single crystals (0.025 g) and RbBr (0.052 g)/CsBr (0.098 g) flux, were used in ion-exchange reaction to obtain single crystals of $[Cs_{6-x}Rb_xBr]NaGa_6Se_{12}$. The furnace containing the tube was ramped up to 650 °C in 3 h, held at this temperature for 24 h, and then cooled to 250 °C at a cooling rate of 10 °C/h. After the reaction and work up in water were complete, the final product was filtered and washed with DI water and acetone. Single crystals of the final product were placed in immersion oil where a $[Cs_{6-x}Rb_xBr]NaGa_6Se_{12}$ single crystal was isolated from $CsGaSe_2$ crystals and mounted for SCXRD. The PXRD pattern for the bulk sample contains $CsGaSe_2$ as the major product and $[Cs_{6-x}Rb_xBr]NaGa_6Se_{12}$ only as a minor phase (Figure S24).

$[Cs_{6-x}K_xBr]KGa_6Se_{12}$. The starting reagents, Ga (0.0540 g), Se (0.1230 g), K_2CO_3 (0.1060 g), in a 1:2:1 molar ratio, and CsBr (0.553 g)/CsI (0.675 g) flux, were used to grow single crystals of $[Cs_{6-x}K_xBr]KGa_6Se_{12}$. The furnace containing the tube was ramped up to 550 °C for 2 h, held at this temperature for 24 h, and then cooled to 250 °C at a cooling rate of 5 °C/h. After the reaction and work up in water were complete, the final product was filtered and washed with DI water and acetone. Single crystals of $[Cs_{6-x}K_xBr]KGa_6Se_{12}$ were placed in immersion oil and mounted for SCXRD. The PXRD pattern for the bulk sample matches the simulated pattern obtained from SCXRD (Figure S25).

$[Cs_6X]AGa_6Q_{12}$:Mn^{2+}. The starting reagents, Ga (0.0540 g), Q, A_2Q, or A_2CO_3 in a 1:2:1 molar ratio, Mn (0.0004, 0.0026, or 0.0052 g or 6, 36, or 72 mol % Mn per F.U., respectively), and a eutectic CsX/CsI mixture (~1.5 g), were used to grow Mn^{2+}-doped single crystals of $[Cs_{6-x}A_xX]AGa_6Q_{12}$. The furnace containing the tube was ramped up to 650 °C in 3 h, held at this temperature for 24 h, and then cooled to 250 °C at a cooling rate of 10 °C/h. After the reaction and work up in water were complete, the final product was filtered and washed with DI water and acetone. The PXRD patterns for the bulk $[Cs_6Cl]NaGa_6S_{12}$:Mn^{2+} samples match well with the simulated pattern obtained from SCXRD of undoped samples (Figures S26 and S27). While the entire sample was ground and this powder was used in

scintillation experiments, large single crystals (>100-μm size) were picked for photoluminescence measurements.

For $[Cs_6Cl]NaGa_6S_{12}$:Mn^{2+}, $[Cs_{6-x}Na_xBr]NaGa_6S_{12}$:$Mn^{2+}$, $[Cs_{6-x}K_xBr]KGa_6S_{12}$:$Mn^{2+}$, and $[Cs_{6-x}Rb_xCl]RbGa_6S_{12}$:$Mn^{2+}$ single crystals, the Mn concentration was determined using ICP-MS (Table S9). For ICP-MS analysis, a sample was sonicated for 1 min in water, followed by decantation. This process was repeated three times. To eliminate the crystal size effect on Mn concertation, the obtained crystals of $[Cs_6Cl]NaGa_6S_{12}$:Mn^{2+}, $[Cs_{6-x}Na_xBr]NaGa_6S_{12}$:$Mn^{2+}$, and $[Cs_{6-x}Rb_xCl]RbGa_6S_{12}$:$Mn^{2+}$ were separated with 355, 100, and 100 μm sieves, respectively. The $[Cs_{6-x}K_xBr]KGa_6S_{12}$:$Mn^{2+}$ sample was submitted for ICP-MS analysis as is due to the small amount of crystals left even after the 100 μm sieving. Additional crystal picking was applied to $[Cs_6Cl]NaGa_6S_{12}$:Mn^{2+} with the highest Mn-loading (72 mol % according to reaction stoichiometry) due to the presence of needle-shaped $Cs_2Mn_3S_4$ single crystals in the sample.

$[Cs_{6-x}Na_xBr]NaGa_6S_{12}$:$Mn^{2+}$ Obtained through Ion Exchange. The starting reagents, $[Cs_{6-x}Na_xBr]NaGa_6S_{12}$ single crystals (0.025 g), $MnCl_2$ (0.001 g), and CsBr (0.033 g)/CsI (0.042 g) flux, were used in an ion-exchange reaction to obtain single crystals of $[Cs_{6-x}Na_xBr]NaGa_6S_{12}$:$Mn^{2+}$. The furnace containing the tube was ramped up to 600 °C for 3 h and held at this temperature for 12 h, and then the furnace was turned off. After the reaction and work up in water were complete, the final product was filtered and washed with DI water and acetone. The final product was placed in immersion oil where a $[Cs_{6-x}Na_xBr]NaGa_6S_{12}$:$Mn^{2+}$ single crystal was isolated from the minor product, $Cs_4Ga_6S_{11}$ crystals, and mounted for microphotoluminescence studies. When larger amounts of $MnCl_2$ (0.002 g) and/or CsBr/CsI flux (0.150 g) are used in the ion-exchange reaction, it results in only the formation of $Cs_4Ga_6S_{11}$.

$[Cs_{6-x}Rb_xCl]RbGa_6S_{12}$:$Mn^{2+}$ Obtained through Ion Exchange. The starting reagents, $[Cs_{6-x}Rb_xCl]RbGa_6S_{12}$ single crystals (0.0125 g), $MnCl_2$ (0.001 g), and CsCl (0.030 g)/CsI (0.045 g), flux were used in an ion-exchange reaction to obtain single crystals of $[Cs_{6-x}Rb_xCl]RbGa_6S_{12}$:$Mn^{2+}$. The furnace containing the tube was ramped up to 600 °C for 3 h and held at this temperature for 12 h, and then the furnace was turned off. After the reaction and work up in water were complete, the final product was filtered and washed with DI water and acetone. The final product was placed in immersion oil where a $[Cs_{6-x}Rb_xCl]RbGa_6S_{12}$:$Mn^{2+}$ single crystal was isolated from the major product, $Cs_4Ga_6S_{11}$ crystals, and mounted for microphotoluminescence studies. When larger amounts of $MnCl_2$ (0.002 g) and/or CsCl/CsI flux (0.150 g) are used in the ion-exchange reaction, it results in only the formation of $Cs_4Ga_6S_{11}$.

$[Cs_6Cl]NaGa_6S_{12}$:Ce^{3+}. The starting reagents, Ga (0.0540 g), S, Na_2S in a 1:2:1 molar ratio, Ce_2S_3 (0.0090 g or 36 mol % Ce per F.U.) and CsCl (0.657 g)/CsI (1.012 g) flux, were used to grow Ce^{3+}-doped single crystals of $[Cs_6Cl]NaGa_6S_{12}$. The furnace containing the tube was ramped up to 650 °C in 3 h, held at this temperature for 24 h, and then cooled to 250 °C at a cooling rate of 10 °C/h. After the reaction and work up in water were complete, the final product was filtered and washed with DI water and acetone. For the $[Cs_6Cl]NaGa_6S_{12}$:Ce^{3+} sample, the Ce concentration was determined using ICP-MS (Table S9). For ICP-MS analysis, a sample was sonicated for 1 min in water followed by decantation. This process was repeated three times. The obtained crystals of $[Cs_6Cl]NaGa_6S_{12}$:Ce^{3+} were separated with a 355 μm sieve.

$[Cs_6Cl]NaGa_6S_{12}$:Eu^{2+}. The starting reagents, Ga (0.0540 g), S (0.0500 g), Na_2S (0.0600 g) in a 1:2:1 molar ratio, Eu_2O_3 (0.0164 g or 72 mol % Eu per F.U.) and CsCl (0.657 g)/CsI (1.012 g) flux, were used to grow Eu^{2+}-doped single crystals of $[Cs_6ClNaGa_6S_{12}$. The furnace containing the tube was ramped up to 650 °C in 3 h, held at this temperature for 24 h, and then cooled to 250 °C at a cooling rate of 10 °C/h. After the reaction and work up in water were complete, the final product was filtered and washed with DI water and acetone. For the $[Cs_6Cl]NaGa_6S_{12}$:Eu^{2+} sample, the Eu concentration was determined using ICP-MS (Table S9). For ICP-MS analysis, a sample was sonicated for 1 min in water followed by decantation. This process was repeated three times. The obtained crystals of $[Cs_6Cl]NaGa_6S_{12}$:Eu^{2+} were submitted for ICP-MS analysis as is due to a small amount of crystals left after sieving.

Mn Concentration in $[Cs_6Cl]NaGa_6S_{12}$:Mn^{2+} Samples. Using the direct synthesis and similar synthetic conditions utilized for $[Cs_6Cl]NaGa_6S_{12}$ crystal growth, we obtained single crystals of $[Cs_6Cl]NaGa_6S_{12}$:$Mn^{2+}{}_{0.03}$, $[Cs_6Cl]NaGa_6S_{12}$:$Mn^{2}{}_{0.04}$, and $[Cs_6Cl]NaGa_6S_{12}$:$Mn^{2+}{}_{0.06}$ where the Mn concentration was determined by ICP-MS on single crystals with >355 μm size. Interestingly, doping with Mn clearly reduced the concentration of Na and Ga (Figure 6), which is consistent with the assigned Mn^{2+}-luminescence resulting from doping on the Na and Ga sites. Moreover, during our ICP-MS analysis, we found that the concertation of Mn depends significantly on the crystal size (Table S9). For the bulk PXRD-pure $[Cs_6Cl]NaGa_6S_{12}$:$Mn^{2+}{}_y$ samples (Figures S26 and S27), the Mn concentration was determined to be $y = 0.01$ and 0.13, while for large single crystals, a Mn loading of $y = 0.03$ and 0.04, respectively, was determined. Thus, large single crystals were used for photoluminescence studies, while the entire ground sample was used for scintillation measurements.

X-ray Crystal Structure Determination. ***$[Cs_6F]NaGa_6S_{12}$, $[Cs_6Cl]NaGa_6S_{12}$, $[Cs_6Cl]NaGa_6Se_{12}$, and $[Cs_6Br]NaGa_6Se_{12}$.*** The compounds crystallize in the rhombohedral crystal system space group $R{-}3m$. The asymmetric unit consists of one Cs atom, one Na atom, one halogen X (X = F, Cl or Br), one Ga atom, and two chalcogen atoms Q (Q = S or Se). The largest residual electron density peak in the final difference map is 0.58/0.71/0.90/0.60 $e^-/Å^3$, located 0.91/0.60/0.74/0.69 Å from Cs1/Cs1/Cs1/Cs1, respectively. The crystallographic data and results of the diffraction experiments are summarized in Tables S1−S4.

$[Cs_{6-x}K_xCl]KGa_6S_{12}$, $[Cs_{6-x}Rb_xCl]RbGa_6S_{12}$, $[Cs_{6-x}Na_xBr]NaGa_6S_{12}$, $[Cs_{6-x}K_xBr]KGa_6S_{12}$, $[Cs_{6-x}Rb_xBr]RbGa_6S_{12}$, $[Cs_{6-x}K_xCl]KGa_6Se_{12}$, $[Cs_{6-x}Rb_xBr]NaGa_6Se_{12}$, and $[Cs_{6-x}K_xBr]KGa_6Se_{12}$. The compounds crystallize in the rhombohedral crystal system space group $R{-}3m$. The asymmetric unit consists of one Cs atom, two alkali atoms A (A = Na, K, or Rb), one halogen X (X = Cl or Br), one Ga atom, and two chalcogen atoms Q (Q = S or Se). In contrast to the $[Cs_6X]NaGa_6Q_{12}$ structures, the Cs site exhibited disorder of the Cs and A cations. To model the Cs1/$A$2 disorder, FVAR and EADP commands were applied, while the coordinates of the A metal were freely refined, i.e., no EXYZ restriction for Cs1/$A$2. Therefore, the occupancy for Cs1 was refined to 0.9276(6)/0.899(8)/0.9486(17)/0.873(3)/0.819(5)/0.957(4)/0.747(4)/0.929(2). For the $[Cs_{6-x}Na_xBr]NaGa_6S_{12}$ structure, the Br atom position was split into two crystallographic sites, resulting in two Br atoms in the asymmetric unit. The occupancy of the Br sites was refined to 0.03 (degeneracy of 6) and 0.82. Introducing the disorder to the crystal structure solution model resulted in a decrease in the R-factor from 0.2% ($[Cs_{6-x}K_xCl]KGa_6Se_{12}$) up to 1.5% ($[Cs_{6-x}Na_xBr]NaGa_6S_{12}$). At the same time, modeling the disorder in the non-salt-inclusion A crystallographic site with A/Cs metals did not lead to a stable refinement. The largest residual electron density peak in the final difference map is 0.35/0.97/0.63/0.54/0.58/0.75/1.02/0.47 $e^-/Å^3$, located 0.82/0.60/0.68/0.76/0.64/0.70/0.87/0.44 Å from Cl1/Cs1/Na2/Cs1/Cs1/Cl1/Cs1/Br1, respectively. The crystallographic data and results of the diffraction experiments are summarized in Tables S1−S4.

■ RESULTS AND DISCUSSION

Structure of $[Cs_6X]AGa_6Q_{12}$. Exploratory flux crystal growth in the Ga−Cs−Q−A−X systems (Q = S and Se; A = Na, K, and Rb; X = Cl and Br) resulted in the discovery of a new family of SICs, $[Cs_6X]AGa_6Q_{12}$ (X = Cl and Br; A = Na, K, and Rb; Q = S and Se, Tables S1−S4). The $[Cs_6X]AGa_6Q_{12}$ structure (sp. gr. $R{-}3\ m$) consists of 2D $[Ga_6Q_{12}]_n{}^{6n-}$ honeycomb layers with embedded zero-dimensional (0D) $[Cs_6X]^{5+}$ salt-inclusion fragments and non-salt-inclusion A^+ cations between the layers (Figure 1). Despite the significant differences in ionic radii between Na, K, and Rb, all studied compositions crystallize in the $R{-}3m$ space group. The framework is built up from Ga_3Q_9 units consisting of cornersharing GaQ_4 tetrahedra. Such Ga_3Q_9 units were previously observed in the 3D anionic framework of $[LiCs_2Cl]LiGa_3S_6$,[49] which differs from the framework in our $[Cs_6X]AGa_6Q_{12}$ material by virtue of the connectivity of the Ga_3Q_9 units. In $[Cs_6X]AGa_6Q_{12}$, each GaQ_4 belonging to a Ga_3Q_9 trimer is further connected *via* edge-sharing to a GaQ_4 that is part of an adjacent Ga_3Q_9 unit, resulting in the formation of a honey-comb layer with 9 Å diameter pore sizes. Although similar honeycomb layers were previously reported for $[Cs_6Cl]GeGa_5Q_{12}$, in the $[LiCs_2Cl]LiGa_3S_6$ structure, the Ga_3Q_9 trimers create a 3D framework.

The $[Cs_6X]AGa_6Q_{12}$ structure is centrosymmetric as two trimeric Ga_3Q_9 units connected through edge-sharing GaQ_4 tetrahedra create an inversion center. The structure consists of $[Ga_6Q_{12}]_n^{6n-}$ honeycomb layers that contain positively charged salt-inclusion octahedra $[Cs_6X]^{5+}$ in the center of the hexagonal pores. These honeycomb layers stack in an ABC fashion, where each successive layer is shifted by $a/3$ relative to the previous one (Figure S28), allowing the non-salt inclusion A cations to occupy the octahedral sites between the layers. This is in contrast with the previously reported $[Cs_6Cl]GeGa_5Q_{12}$ structure (sp. gr. $R\text{–}3m$) in which, due to the substitution of one Ga^{3+} for one Ge^{4+} cation per formula unit, the isotypic $[GeGa_5Q_{12}]_n^{5n-}$ layers do not require the A^+ cations for charge balance leaving empty octahedral sites.[75]

Alkali Cation Size Effects. The $[Cs_6Cl]NaGa_6S_{12}$, $[Cs_6Cl]NaGa_6Se_{12}$, and $[Cs_6Br]NaGa_6Se_{12}$ compositions have fully ordered salt inclusions, resulting in the $[Cs_6X]AGa_6Q_{12}$ formula, while the remainder of the compositions reported herein exhibit Cs and A cation mixing on the salt inclusion site (Figure 2), resulting in compositions of the type $[Cs_{6-x}A_xX]AGa_6Q_{12}$ (Figures S29–S32). For example, in the $[Cs_{6-x}A_xCl]AGa_6S_{12}$ series, we observe Cs/A mixing ranging from zero to 10% (Figure 2a). This trend correlates with the A cation radii, i.e., the 9-coordinated A metal radii (Figure S33) increase from 1.24 to 1.63 Å from Na to Rb, resulting in a better match between the sizes of the A and Cs cations (1.78 Å for 9-coordinated Cs). The same trend is observed for the $[Cs_{6-x}A_xBr]AGa_6S_{12}$ (Figure 2b) and $[Cs_{6-x}A_xX]AGa_6Se_{12}$ (X = Cl and Br) series (Figure 2c). Interestingly, both the X and Q anions also affect the extent of Cs/A site mixing, which increases for the Br over the Cl compositions and decreases for the Se over the S compositions; in contrast, the non-salt-inclusion sites in all these series do not exhibit site mixing.

a) salt-inclusion moiety in $[Cs_{6-x}A_xCl]AGa_6S_{12}$

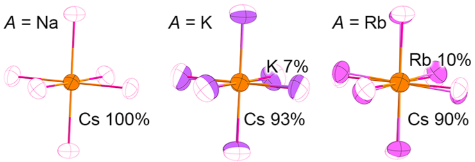

b) x in $[Cs_{6-x}A_xX]AGa_6S_{12}$

X \ A	Na	K	Rb
Cl	0.3	0.8	–
Br	0.0	0.4	0.6

c) x in $[Cs_{6-x}A_xX]AGa_6Se_{12}$

X \ A	Na	K	Rb
Cl	0.0	0.4	–
Br	0.0	0.3	–

Figure 2. (a) View of salt the inclusion moiety in $[Cs_{6-x}A_xCl]AGa_6S_{12}$. Orange, violet, pink, and white ellipsoids present Cl, K, Rb, and Cs atoms, respectively. x in (b) $[Cs_{6-x}A_xX]AGa_6S_{12}$ and (c) $[Cs_{6-x}A_xX]AGa_6Se_{12}$ as a function of A and X.

Flux Influence on the Formation of SIC Materials. Multiple parameters affect the formation of SICs, e.g., the halide salt, the framework building block, the temperature profile, and the choice of flux. To better understand the formation of GaQ_4-based SICs, we analyzed the 39 reported GaQ_4-based frameworks.[49−54,56,57,72,74,75,88−95] The data in Tables S10 and S11 reveal that polychalcogenide flux crystal growth can be successfully coupled with halide fluxes to obtain single crystals of SICs. The polychalcogenide flux, over a wide range of temperatures, appears to increase the solubility and reactivity of the chalcogenide reagents and intermediates, consistent with hard-soft principles.[96] Furthermore, in addition to the direct use of A_2Q_n polychalcogenide fluxes, there are examples of alternative synthetic routes that involve the *in situ* generation of the polychalcogenide flux. For instance, a combination of elemental Q and A_2Q (A = alkali) or $A'Q$ (A' = alkali earth), a reaction between Q and A/A' metal, or, less common, the reaction between a carbonate salt $A_2CO_3/A'CO_3$ with Q (Q = S and Se).[51,75,89,92] As detailed in Tables S10 and S11, most of the GaQ_4-based SICs were synthesized using the first two methods, and so far, the use of carbonates has not been reported for synthesizing SICs. Interestingly, the identity of the cation in the flux also influences the formation of the specific framework building block. For instance, Ba-based fluxes tend to stabilize 0D GaQ_4 isolated units in SIC,[89−91,95] while combinations of Ba-based fluxes with K/Rb/Cs-containing salts typically yield GaQ_4 and Ga_4Q_{10} framework building units.[50,52,54,57] The formation of new framework moieties, including Ga_3Q_9, MGa_3Q_{10}, MQ_4, and MQ_6, tends to take place when Li, B, or M (P, 3d element, Ge, Cd, and In) metals are added to the reaction mixture.[49,51,53,56,72,74,75,88,93,94] For example, $[Cs_6Cl]_6Cs_3Ga_{53}Se_{96}$, which contains the Ga_3Q_9 unit, could be synthesized only upon the addition of Mn metal to the reaction mixture.[74] Similarly, for the synthesis of $[LiCs_2Cl]LiGa_3S_6$, which also contains Ga_3Q_9 trimers, both Li and Ba metals are combined in the reaction mixture; the use of only Li metal did not lead to the target phase.[49] Finally, $[Cs_6Cl]GeGa_5Q_{12}$ (Q = S and Se), which contains $(Ga/Ge)_3Q_9$ trimer-based $[GeGa_5Q_{12}]_n^{5n-}$ layers, isotypic to those in $[Cs_6X]AGa_6Q_{12}$, was crystallized from a CaQ/CsCl flux.[75]

We can make general observations based on the data in Tables S10 and S11, which suggest that GaQ_4-based SICs with 0D XCs_6 units form when a CsX salt is used in the reaction without the addition of Ba metal.[74,75,88] In contrast, the use of a Ba-only based flux stabilizes XBa_4 (X = F and Cl) tetrahedra or XBa_6 (X = Cl, Br, and I) octahedra that form 2D or 3D salt-inclusion moieties.[53,56,72,89−91,95] The formation of other salt-inclusion building blocks is possible when the flux contains only A cations (A = Na and K)[92−94] or a combination of Ba and A metal (A = Li, K, Rb, and Cs).[49−52,54,57] In summary, for the GaQ_4-based SIC materials, we find that flux, salt-inclusion, and framework building blocks all influence the phase formation of SICs, illustrating how complex the synthesis of SICs is.

In this study, we did not use Ba-based fluxes, which are mainly utilized for the synthesis of GaQ_4-based SICs. Instead, we explored alkali-metal-based fluxes, specifically those involving a combination of two metals. A reaction between Ga, A_2Q/A_2CO_3, Q, and CsX/CsI (see the Experimental Section for more details) resulted in colorless hexagonal crystals of $[Cs_6X]$

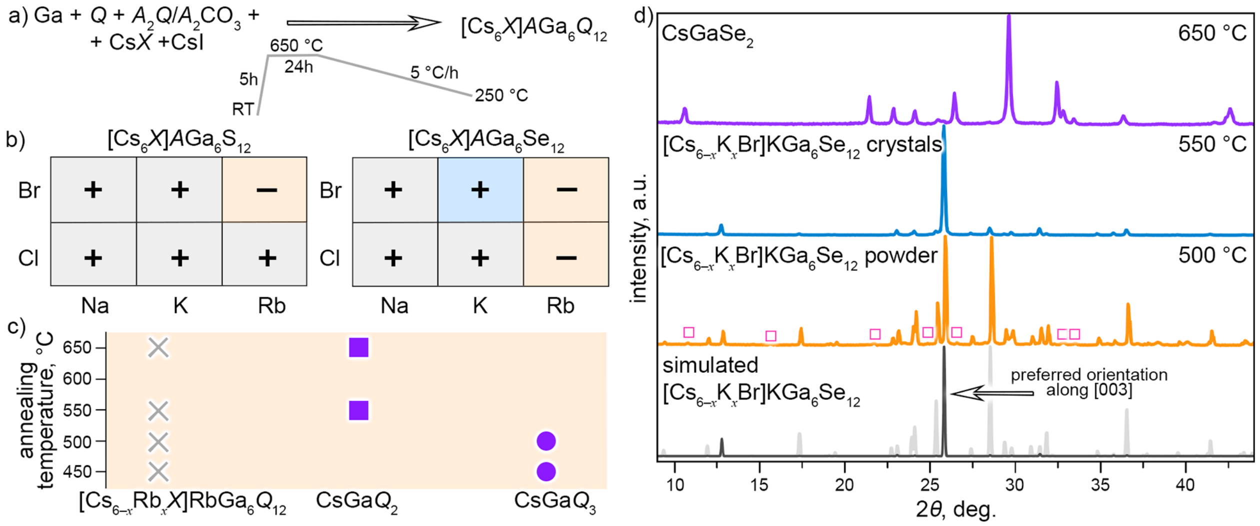

Figure 3. (a) Reaction scheme for $[Cs_6X]AGa_6Q_{12}$ crystal growth. (b) Composition map of the $[Cs_6X]AGa_6Q_{12}$ structure. Gray, blue, and orange color highlight whether single crystals were synthesized at an annealing temperature of 650 °C, < 650 °C, or were not obtained even in the 450−650 °C temperature range, respectively. (c) Phase composition of the reaction targeting $[Cs_{6-x}Rb_xBr]RbGa_6S_{12}$ and $[Cs_{6-x}Rb_xX]RbGa_6Se_{12}$ (X = Cl and Br) at different temperatures. (d) PXRD patterns of the products of the reaction targeting $[Cs_{6-x}K_xBr]KGa_6Se_{12}$ at 500 °C (orange), 550 °C (blue), and 650 °C (violet); and $[Cs_{6-x}K_xBr]KGa_6Se_{12}$ simulated with (black) and without preferred orientation along [003] (gray). Pink squares highlight the impurity phase, which was not identified.

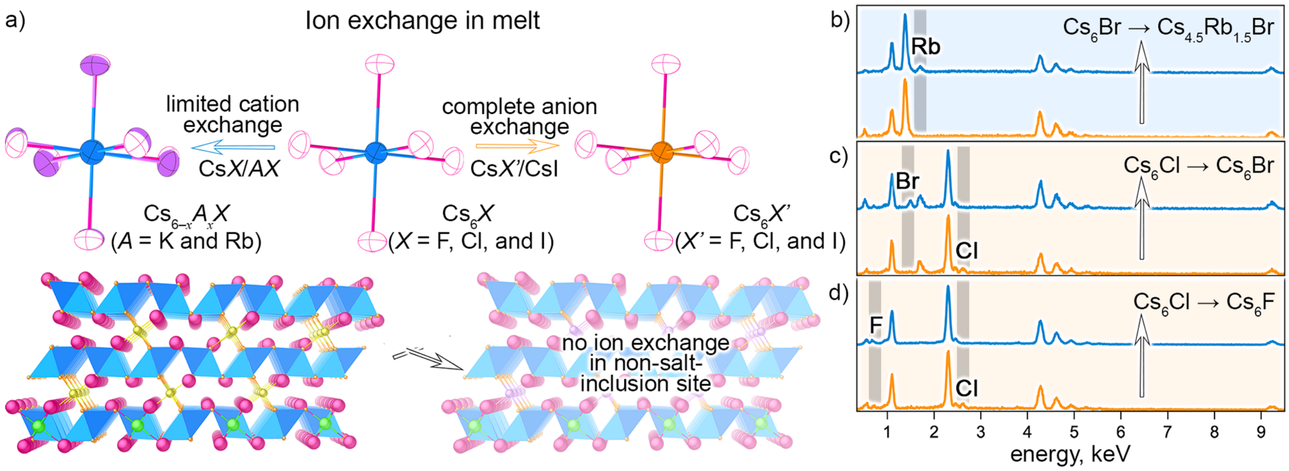

Figure 4. (a) Cation- and anion-exchange scheme for (top) salt-inclusion moiety and (bottom) non-salt-inclusion site. EDS spectra of starting SIC crystal (orange) and ion-exchanged product (blue) in reaction (b) $[Cs_6Br]NaGa_6Se_{12} \rightarrow [Cs_{6-x}Rb_xBr]NaGa_6Se_{12}$, (c) $[Cs_{6-x}Rb_xCl]RbGa_6S_{12} \rightarrow [Cs_{6-x}Rb_xBr]RbGa_6S_{12}$, and (d) $[Cs_6Cl]NaGa_6S_{12} \rightarrow [Cs_6F]NaGa_6S_{12}$. Blue and orange color highlight cation and anion exchange in a salt-inclusion fragment, respectively. For EDS spectra, peaks for O (0.5 eV); Na (1.0 eV); S (0.5, 2.3, and 2.4 eV); Ga (1.1 and 9.2 eV); Se (1.4 eV); and Cs (0.9, 4.3, 4.6, 4.9, 5.3, and 5.6 eV) are not labeled (Figure S2−S13).

AGa_6Q_{12}, which crystallizes in a new structure type (Figure 1, Tables S1−S4). During heating, A_2CO_3 reacts with sulfur or selenium, leading to the *in situ* formation of the polychalcogenide flux (A_2Q or A_2Q_n), out of which $[Cs_6X]AGa_6Q_{12}$ crystallizes at 650 °C; in the absence of the A_2S/A_2CO_3 reagents, only Ga_2S_3 and S_8 powder products are isolated.

Synthesis Temperature. Temperature is an additional important factor that influences the formation of the $[Cs_6X]AGa_6Q_{12}$ structure. To synthesize the $[Cs_6X]AGa_6Q_{12}$ series, we used a temperature profile with a maximum annealing temperature of 650 °C (Figure 3a), which enabled the synthesis of many but not of all combinations of X (Cl and Br), A (Na, K, and Rb), and Q (S and Se). For example, the reaction between Ga, K_2CO_3, and Se, in a CsBr/CsI flux at 650 °C leads to the formation of $CsGaSe_2$ (Figure 3b), but decreasing the maximum annealing temperature to 500 °C results in the formation of a polycrystalline powder of $[Cs_{6-x}K_xBr]KGa_6Se_{12}$ (Figure 3d). To obtain hexagonal-plate-shaped single crystals of $[Cs_{6-x}K_xBr]KGa_6Se_{12}$, the optimum annealing temperature was found to be 550 °C. This same strategy, however, failed to yield $[Cs_{6-x}Rb_xBr]RbGa_6S_{12}$ and $[Cs_{6-x}Rb_xX]RbGa_6Se_{12}$ (X = Cl and Br) and resulted only in $CsGaQ_2$ or $CsGaQ_3$ (Figure 3c). This suggests that $[Cs_6X]AGa_6Q_{12}$ is a kinetic phase, which may be stabilized at lower temperatures, as in the case of $[Cs_{6-x}K_xBr]KGa_6Se_{12}$, and competes with the thermodynamic $CsGaQ_2$ phase in the A_2Q_n−CsX−CsI flux.[1]

Thermal Stability of $[Cs_6X]AGa_6S_{12}$. To probe the thermal stability of the $[Cs_6X]AGa_6Q_{12}$ family, we investigated several compositions, including $[Cs_6X]AGa_6S_{12}$ (A = Na, K, and Rb), using DSC coupled with TGA under an N_2 atmosphere. These measurements demonstrated the thermal stability of these compositions up to 700 °C, as confirmed by analyzing post-TGA samples *via* PXRD (Figures S34 and S35). Heating a vacuum-sealed powder sample of $[Cs_6Cl]NaGa_6S_{12}$ to 900 °C for 5 h, followed by quenching, on the other hand, resulted in sample decomposition and the formation of $CsGaS_2$. This is consistent with the formation of $CsGaQ_2$ in $A_2Q_n{-}CsX{-}CsI$ fluxes when the temperature exceeds 700 °C.

Ion Exchange in $[Cs_6X]AGa_6Q_{12}$. The observation of mixed site occupancy in the salt-inclusion $[Cs_{6-x}A_xCl]AGa_6Q_{12}$ demonstrates compositional flexibility and suggests the possibility of preparing additional compositions *via* ion-exchange reactions. The titled sulfur-based compounds are thermally stable up to 700 °C, and the selenium-based materials are assumed to be stable at least up to the maximum annealing temperature used in their synthesis. Those temperatures are sufficient to melt eutectic CsX/AX and CsX/CsI mixtures and to use them for single-crystal-to-single-crystal (SC-SC) ion-exchange reactions. To confirm that ion exchange took place, a combination of EDS and SCXRD was used to verify the changes in the sample compositions and, as needed, to refine the salt inclusion site's mixed cation occupancies.

A series of SC-SC ion-exchange reactions demonstrated that only the salt-inclusion moiety $[Cs_6X]^{5+}$ or $[Cs_{6-x}A_xX]^{5+}$ participate in the ion exchange process and that the non-salt-inclusion cations do not. (Figure 4a). For instance, the rubidium ion exchange into $[Cs_6Br]NaGa_6Se_{12}$ single crystals using a RbBr/CsBr eutectic mixture at 650 °C resulted mostly in $CsGaSe_2$ single crystals (presumably due to thermal decomposition of SIC) and $[Cs_{6-x}Rb_xBr]NaGa_6Se_{12}$ as a minor product (Table S12, Figure 4b and, Figure S24). EDS analysis of $[Cs_{6-x}Rb_xBr]NaGa_6Se_{12}$ crystals supports the ion exchange of Rb into the structure, and SCXRD quantitatively determined that 25% of the Cs cations were substituted by Rb (x = 1.5). Furthermore, SCXRD demonstrated that the ion exchange involved only the $[Cs_6X]^{5+}$ but not the Na crystallographic position. The 25% rubidium/cesium substitution turned out to be the maximum that could be achieved and attempts to increase the exchange fraction simply led to the formation of $CsGaSe_2$. Higher exchange levels may cause the $[Cs_{6-x}A_xX]AGa_6Q_{12}$ structure to become unstable such that the decomposition products enable the crystallization of $CsGaQ_2$ from the melt.

While there is a limited cation exchange in the salt-inclusion moiety, Cl^- anions in $[Cs_{6-x}Rb_xCl]RbGa_6S_{12}$ completely exchanged with Br^- in a CsBr/RbBr melt to form $[Cs_{6-x}Rb_xBr]$-$RbGa_6S_{12}$ (Table S12), as shown by EDS and SCXRD measurements (Figure 4c). Interestingly, we were unable to obtain this composition using flux crystal growth (Figure 3b). Similar SC-SC ion exchange reactions were observed in $[Cs_6Cl]_2Cs_5Ga_{15}Ge_9Se_{48}$, which consists of a 0D super-cuboctahedron covalent building block, 0D $[Cs_6Cl]^{5+}$ salt-inclusion fragment, and Cs ions.[88] Here also, both cation and anion exchange were observed only for the salt-inclusion moiety (Table S12), and ion exchange reactions did not proceed for the non-salt-inclusion cation site. Extending our work to iodine substitutions did not succeed, and we could not introduce I^- into the salt-inclusion of the $[Cs_6X]AGa_6Q_{12}$ structure. This contrasts with $[Cs_6Cl]_2Cs_5Ga_{15}Ge_9Se_{48}$, where the composition $[Cs_6I_{0.6}Cl_{0.4}]_2Cs_5Ga_{15}Ge_9Se_{48}$ was achieved, perhaps due to more accessible diffusion pathways in 0D relative to 2D frameworks.

Extending our work to fluorine, on the other hand, was successful. The synthesis of F-containing SIC compounds is challenging due to the reactivity of crucible materials with F-based fluxes, particularly the corrosive AF (A = Li, Na, K, and Rb) fluxes.[88] For that reason, most F-containing SIC structures were synthesized using the less reactive SrF_2 or BaF_2 fluxes contained in carbon crucibles and sealed in silica tubes.[63,65,66,68−70,72,73,89,97] Since ion-exchange reactions can lead to new compositions that cannot be obtained with traditional synthetic routes, we decided to probe the use of a CsF/CsI flux to obtain $[Cs_6F]NaGa_6S_{12}$ (Figure 4d). For the preparation of $[Cs_6F]NaGa_6S_{12}$, single crystals of $[Cs_6Cl]$-$NaGa_6S_{12}$ were mixed with the flux and placed into a silver tube that was later crimped and sealed inside a carbon-coated silica tube (see the Experimental Section for more details). This succeeded, and both EDS and SCXRD confirmed the substitution of Cl^- by F^- in the crystal structure (Figure 4d). Clearly, ion exchange is a viable route for obtaining new fluoride-based SIC materials that cannot be obtained or are extremely challenging to synthesize *via* traditional synthetic routes.

Theoretical Stability of $[Cs_6X]AGa_6Q_{12}$. To evaluate the thermodynamic stability of different $[Cs_6X]AGa_6Q_{12}$ compositions, we performed DFT calculations to derive their enthalpies of formation. These calculations are based on the idealized compositions and were modeled assuming the absence of any anion or cation disorder. The data in Table S13 clearly shows that all $[Cs_6X]AGa_6Q_{12}$ compositions with X = F, Cl, Br, and I, A = Li, Na, K, Rb, and Cs, Q = S and Se have negative ΔH_f^{0K} and, thus, are in principle stable. Nonetheless, our attempts to incorporate, for example, Li or I into the $[Cs_6X]AGa_6Q_{12}$ structure did not succeed. To consider a reaction profile that could include more stable phases in the $Cs{-}X{-}A{-}Ga{-}Q$ system, we built a convex hull using the OQMD.[84,85] The convex hull helps to determine the most favorable decomposition reaction of $[Cs_6X]AGa_6Q_{12,}$ i.e., the one which has the most thermodynamically stable products in the $Cs{-}X{-}A{-}Ga{-}Q$ landscape keeping the elemental stoichiometry of the $[Cs_6X]AGa_6Q_{12}$ composition.[84,85] According to OQMD, typical $[Cs_6X]AGa_6Q_{12}$ compounds can decompose according to one of two reactions:

$$[Cs_6X]AGa_6Q_{12} \rightarrow 6CsGaQ_2 + AX \tag{1}$$

$$[Cs_6X]AGa_6Q_{12} \rightarrow 5CsGaQ_2 + AGaQ_2 + CsX \tag{2}$$

These reactions are reasonable as we know from our thermal analysis measurements that, for example, $[Cs_6Cl]NaGa_6S_{12}$ decomposes to $CsGaS_2$ and NaCl at high temperatures, which is consistent with the decomposition of $[Cs_6Cl]$-$NaGa_6S_{12}$*via*Reaction 1 predicted by convex hull construction. In this sense, none of the $[Cs_6X]AGa_6Q_{12}$ compounds are stable, and all have a negative decomposition enthalpy at 0 K (Figure 5a,b, Figure S36 and S37, Table S13), supporting the claim that these SICs are kinetically stabilized.

Even though convex hull data favors decompositions of those materials, we attempted to compare $\Delta H_{\mathrm{decom}}^{0K}$ enthalpies for the entire $[Cs_6X]AGa_6Q_{12}$ series (Figures S36 and S37 and Table S13). Less negative $\Delta H_{\mathrm{decom}}^{0K}$ values indicate a smaller thermodynamic driving force for the decomposition reaction. In general, we observed that the thermodynamic stability ranges for $[Cs_6X]AGa_6Q_{12}$ compositions are consistent with experiments showing that the $[Cs_6Cl]^{5+}$ salt-inclusion moiety is more energetically favorable than $[Cs_6Br]^{5+}$ and Na- and K-containing phases are more stable than Rb-ones. For example, in the synthesized $[Cs_6X]AGa_6Se_{12}$ series, $[Cs_6Br]KGa_6Se_{12}$ is the least stable according to DFT calculations (Figure 5) and its disordered analog $[Cs_{6-x}K_xBr]KGa_6Se_{12}$ has to be synthesized at lower temperatures (Figure 3d). Also, we were not able to

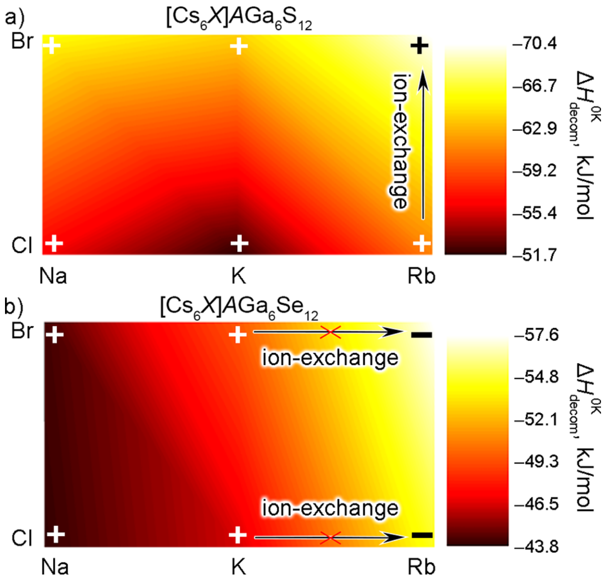

Figure 5. Contour plot of enthalpies of (a) $[Cs_6X]AGa_6S_{12}$ and (b) $[Cs_6X]AGa_6Se_{12}$ decomposition reactions, leading to $CsGaQ_2$ or $AGaQ_2$ and the respective salt, AX or CsX, as a function of A and X.[84,85] Plus and minus schematically demonstrate $[Cs_6X]AGa_6Q_{12}$ compositions, which we were able and were not able to obtain *via* flux crystal growth or ion-exchange reaction, respectively.

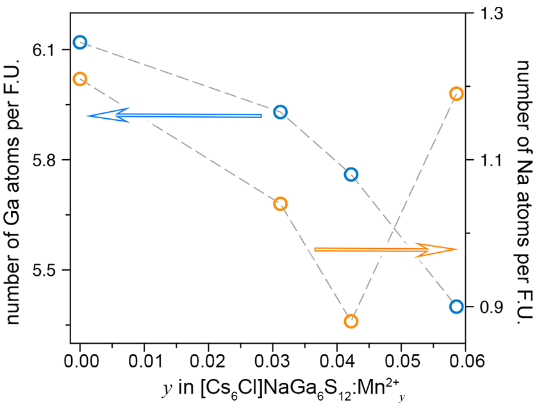

Figure 6. ICP-MS results for $[Cs_6Cl]NaGa_6S_{12}$:Mn^{2+}_y single crystals. Number of Ga (blue circles) and Na (orange circles) per formula unit as a function of y in $[Cs_6Cl]NaGa_6S_{12}$:Mn^{2+}_y.

synthesize $[Cs_{6-x}Rb_xBr]RbGa_6S_{12}$ using traditional flux crystal growth, and DFT calculations show that this composition is the least stable of the $[Cs_6X]AGa_6S_{12}$ series (X = Cl and Br; A = Na, K, and Rb) (Figure 5). In the broader range of $[Cs_6X]AGa_6Q_{12}$ compositions with X = F, Cl, Br, and I, A = Li, Na, K, Rb, and Cs, Q = S and Se, we found that DFT calculations were in line with experiment and highlighted that the synthesized compounds are the most stable (Figures S36 and S37). $[Cs_6X]AGa_6Q_{12}$ compositions with X = F and I or A = Li and Cs have the most negative ΔH^{0K}_{decom} (Figures S36 and S37 and Table S13) and were not synthetically accessible within the synthesis temperatures used. This exercise illustrates that DFT calculations can readily help to predict the stability of new structures, depending on their composition, and help guide the preparation of new phases, even if these phases are kinetic and not thermodynamic product.

Photoluminescence of $[Cs_6X]AGa_6Q_{12}$:Mn^{2+}. The structure of $[Cs_6X]AGa_6Q_{12}$ contains several different coordination environments into which optically active elements can, in principle, be incorporated, making these materials promising hosts for photophysical studies and optical applications. We focused on Mn^{2+}, one of the most popular inorganic dopants whose emission color can vary from green to red as a function of coordination environment and crystal field.[98−106] UV−vis spectroscopy was used to extract a band gap of 4.3 eV for $[Cs_6Cl]NaGa_6S_{12}$, which is acceptable for hosts in solid-state lighting (Figure S38). We utilized two approaches to introduce Mn^{2+} and control the Mn^{2+} content of $[Cs_6X]AGa_6Q_{12}$ single crystals: (1) incorporation of Mn *via* direct synthesis by including a Mn starting reagent and (2) *via* SC-SC ion-exchange reactions using a $MnCl_2$-containing CsX/CsI flux. Using the first method, we obtained single crystals of $[Cs_6X]AGa_6Q_{12}$:Mn^{2+}_y. By adjusting the amount of Mn added to the reaction, we were able to change the dopant level from y = 0.03 to 0.06 Mn per F.U. as determined by ICP-MS (Figure 6 and Table S9, see the Experimental Section for more details). The latter method, SC-SC ion exchange, resulted in partial crystal decomposition to $Cs_4Ga_6S_{11}$ (see the Experimental Section for more details); thus, individual crystals of SIC materials $[Cs_6X]AGa_6Q_{12}$:Mn^{2+} were selected for photoluminescence analysis. A unit cell check conducted on these crystals prior to use confirmed that the $[Cs_6Cl]NaGa_6Q_{12}$:Mn^{2+} crystals retained the structure and space group, $R-3m$.

Photoluminescence data were collected on individual single crystals of $[Cs_6X]AGa_6Q_{12}$:Mn^{2+}. Measuring the luminescence of crystals obtained by direct synthesis resulted in bright emission ranging from orange (∼610 nm) to red (∼690 nm) for $[Cs_6Cl]NaGa_6S_{12}$:Mn^{2+}. In contrast, no luminescence was observed for $[Cs_6Cl]NaGa_6S_{12}$:Mn^{2+} single crystals obtained *via* a SC-SC ion-exchange reaction. $Mn^{2+}(3d^5)$-luminescence is associated with a partially forbidden transition from the $^4T_{1(g)}$ (G) excited state to the $^6A_{1(g)}$ (S) ground state. According to the d^5 Tanabe−Sugano diagram, the $^4T_1 \rightarrow {}^6A_1$ transition in a weak tetrahedral crystal field, i.e., in MnQ_4, has a larger energy transition than the $^4T_{1(g)} \rightarrow {}^6A_{1(g)}$ transition in an octahedral crystal field for MnQ_6.[98,105] In addition to the ligand identity and coordination number, another significant factor affecting the crystal field is the size mismatch between the dopant and host framework site, which ultimately can be considered a chemical pressure applied to Mn^{2+} to fit into the host matrix (Figure 7a).[107] For example, Mn doping into rock salt MS (M = Mg, Ca, Sr., and Ba) leads to a photoluminescence peak shift of over ∼150 nm (Figure 7b), even though all MS:Mn^{2+} compositions contain only one type of octahedral MnS_6 luminescent center.[101−104] The more significant the radii mismatch, $\frac{r(M) - r(\mathrm{Mn})}{r(M)} \times 100\%$, (Table S14), the more prominent the MnS_6-luminescence blue-shift is. A similar trend was observed for MnS_4 tetrahedral fluorescence centers in ZnS and Ga_2S_3 samples (Figure 7c and Table S14).[107,108]

Based on these literature reports, we speculate that the lower wavelength peak in $[Cs_6Cl]NaGa_6S_{12}$:Mn^{2+} luminescence (∼610 nm) originates from Mn doping into the octahedral site (GaS_6), while the GaS_4 tetrahedral site doping results in a ∼690 nm emission (Figure 8a); this matches well with observed Mn^{2+} luminescence in the Ga_2S_3 structure, i.e., 685 nm.[108] The radii mismatch between Mn^{2+} and the Na and the Ga host sites differs significantly and is plus 18.6% and minus 40.4%, respectively (Table S14). Based on the collected luminescence data, it appears that Mn^{2+} preferentially occupies the NaS_6 site under low Mn reactant content. For higher Mn reactant content,

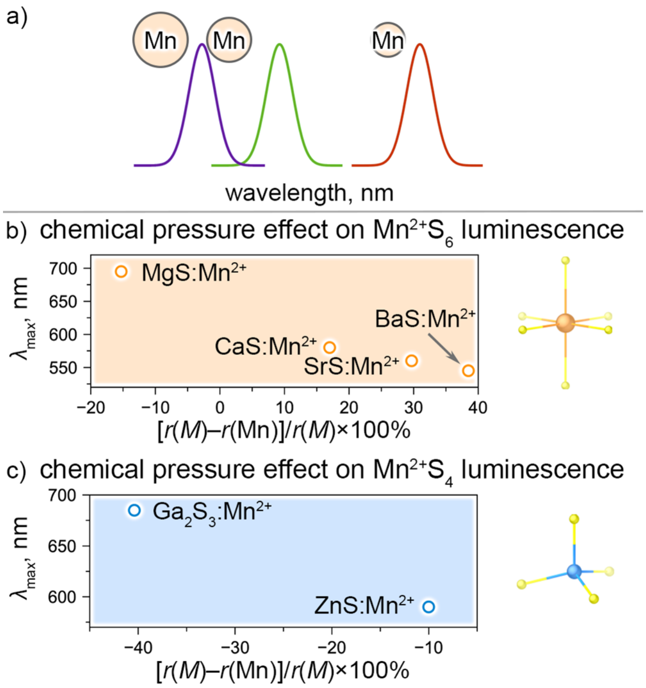

Figure 7. (a) Schematic representation of radii mismatch effect on Mn^{2+}-luminescence. The emission peak position for (b) MnS_6[101−104] and (c) MnS_4[107,108] as a function of a radii mismatch between *M* cation, host crystallographic site, and Mn, dopant.

it also starts to occupy the GaS_4 site. This hypothesis is in good agreement with the experiment, where at low Mn concentration, the material emits at ∼610 nm − orange, Figure 8a; for medium Mn concentrations, it luminesces equally at ∼610 and ∼690 nm (Figure 8a); while for the highest Mn concertation, the single crystals luminesce most at ∼690 nm (red), as more of the gallium site is occupied by Mn (Figure 8a).

Our analysis of the luminescence behavior of $[Cs_6X]AGa_6Q_{12}:Mn^{2+}$ (Figures S39−S48) demonstrated that the *X* and *Q* anions in $[Cs_6X]AGa_6Q_{12}:Mn^{2+}$ have almost no effect on the emission spectra (Figure 8c,d). In contrast, a change in the *A* cation leads to a significant difference in the luminescence brightness, dropping in intensity from Na to K/Rb analogs, as well as in the number of peaks and their positions (Figure 8b). Changing from Na to K and Rb, the size mismatch increases to 39.9% and 45.4%, respectively (Table S14), and hence the peak at ∼610 nm disappears from photoluminescence spectra (Figure 8b). In contrast, the peak corresponding to the Ga site doping at ∼690 nm is still present. It is worth noting that there is also a distortion of the GaQ_4 and AQ_6 polyhedra within the $[Cs_6X]AGa_6Q_{12}$ structures (Tables S5−S7), which likely also impacts the photoluminescence.[109−112] However, we did not study this aspect.

Our SC-SC ion exchange experiments described earlier demonstrated that we can only ion exchange the Cs cations in the salt-inclusion fragment and are not able to introduce cations into the actual framework. In the case of SC-SC ion exchange for mixed alkali metal salt-inclusions, such as $[Cs_{6-x}A_xX]AGa_6Q_{12}$, it is possible to introduce additional, non-framework Mn^{2+} luminescent centers into the salt-inclusion fragment. We speculate that this can occur due to the better size match of Mn^{2+} with A^+ (A = Na, K, and Rb) cations versus Cs^+. Single crystals of such modified compositions, $[Cs_{6-x}A_xX]AGa_6Q_{12}:Mn^{2+}$, exhibit additional ∼500 nm and ∼ 560 nm

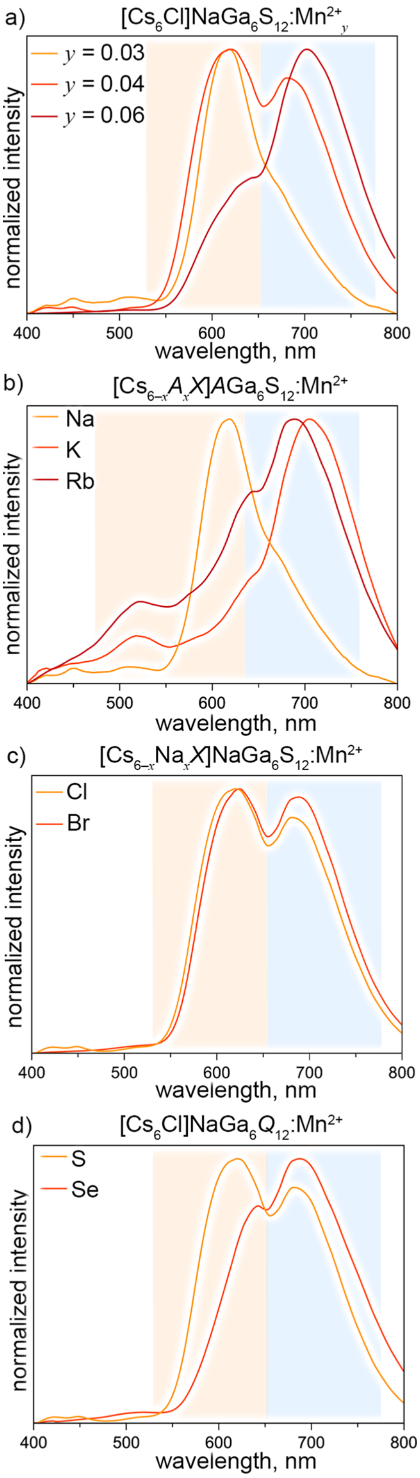

Figure 8. Normalized photoluminescence spectra of single crystals of (a) $[Cs_6Cl]NaGa_6S_{12}:Mn^{2+}_{0.03}$ (orange), $[Cs_6Cl]NaGa_6S_{12}:Mn^{2+}_{0.04}$ (red), and $[Cs_6Cl]NaGa_6S_{12}:Mn^{2+}_{0.06}$ (dark red); (b) $[Cs_6Cl]NaGa_6S_{12}:Mn^{2+}_{0.03}$ (orange), $[Cs_{6-x}K_xBr]KGa_6S_{12}:Mn^{2+}_{0.04}$ (red), and $[Cs_{6-x}Rb_xCl]RbGa_6S_{12}:Mn^{2+}_{0.01}$ (dark red); (c) $[Cs_6Cl]NaGa_6S_{12}:Mn^{2+}_{0.04}$ (orange) and $[Cs_{6-x}Na_xBr]NaGa_6S_{12}:Mn^{2+}_{0.01}$ (red); and (d) $[Cs_6Cl]NaGa_6S_{12}:Mn^{2+}$ (orange) and $[Cs_6Cl]NaGa_6Se_{12}:Mn^{2+}$ (red). All emission spectra were collected on single crystals using a HORIBA Scientific Standard Microscope Spectroscopy System with a 375 nm laser excitation source. Orange and blue color highlight Mn^{2+}-luminescence in the octahedral and tetrahedral environments, respectively.

centered emissions and lead to more complex spectra. As a result, $[Cs_{6-x}Na_xBr]NaGa_6S_{12}:Mn^{2+}$ and $[Cs_{6-x}Rb_xCl]RbGa_6S_{12}:Mn^{2+}$ single crystals exhibit essentially white emission under 375 nm laser excitation (Figure 9). These spectra are noticeably different from the spectra collected for $[Cs_{6-x}Na_xBr]NaGa_6S_{12}:Mn^{2+}$ (Figure 9a) and $[Cs_{6-x}Rb_xCl]RbGa_6S_{12}:Mn^{2+}$ (Figure 9b) synthesized *via* direct synthesis, offering additional pathways for tuning the optical properties of SIC materials.

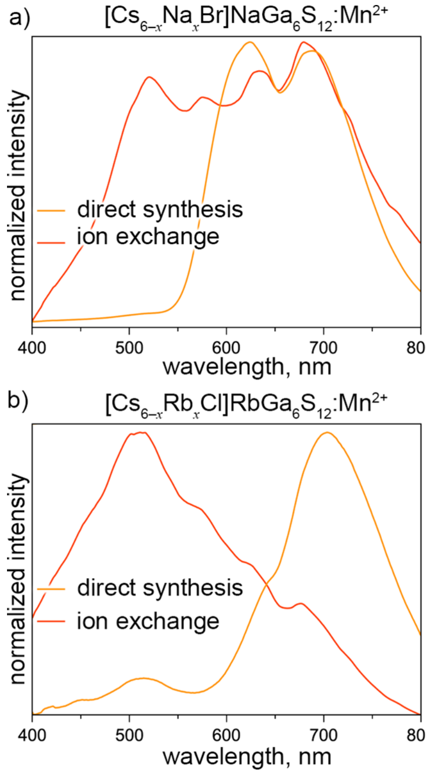

Figure 9. Normalized photoluminescence spectra of single crystals of (a) $[Cs_{6-x}Na_xBr]NaGa_6S_{12}:Mn^{2+}$ and (b) $[Cs_{6-x}Rb_xCl]RbGa_6S_{12}:Mn^{2+}$ obtained through direct synthesis (orange) and ion exchange (red). All emission spectra were collected on single crystals using a HORIBA Scientific Standard Microscope Spectroscopy System with a 375 nm laser excitation source.

Finally, to demonstrate the versatility of $[Cs_6X]AGa_6Q_{12}$ structure for creating new optical materials, we also explored doping with other popular luminescence centers, such as Ce^{3+} and Eu^{2+}, which resulted in the typical blue and green emissions, respectively (see the Experimental Section for more details, Figures S49−S51).[113−122]

Scintillation of $[Cs_6Cl]NaGa_6S_{12}:Mn^{2+}$. The photoluminescent properties of $[Cs_6X]AGa_6Q_{12}:Mn^{2+}$ inspired us to test whether these materials exhibit scintillation.[123−127] Single crystals of $[Cs_6X]AGa_6S_{12}:Mn^{2+}$ were irradiated by X-rays inside a diffractometer equipped with a copper X-ray source while monitoring their emission using a digital camera (Figure 10a and Figures S39−S44). All $[Cs_6X]NaGa_6S_{12}:Mn^{2+}$ crystals demonstrated bright orange scintillation, while $[Cs_{6-x}K_xBr]KGa_6S_{12}:Mn^{2+}$ and $[Cs_{6-x}Rb_xCl]RbGa_6S_{12}:Mn^{2+}$ did not scintillate. Radioluminescence of $[Cs_6Cl]NaGa_6S_{12}:Mn^{2+}{}_{0.01}$ and $[Cs_6Cl]NaGa_6S_{12}:Mn^{2+}{}_{0.13}$ bulk samples (Figures S26 and S27, Table S9) were measured using a dedicated spectrometer (see the Experimental Section for more details) and produced scintillation centered at 610 nm (Figure 10a). The integrated brightness of $[Cs_6Cl]NaGa_6S_{12}:Mn^{2+}{}_{0.01}$ and $[Cs_6Cl]NaGa_6S_{12}:Mn^{2+}{}_{0.13}$, was estimated to be 22% and 9%, respectively, that of a commercial scintillator, bismuth germanium oxide (BGO). The higher Mn content resulted in a decrease in the material's scintillation, presumably due to concentration quenching.[126,128,129] In the future, efficiency improvements can be explored by optimizing Mn concentration in $[Cs_6X]NaGa_6S_{12}:Mn^{2+}$ since a clear dependence on the Mn content was observed (Figure 10a). Sulfur-based materials, compared to oxides, are thought to have better attenuation length characteristics for scintillators due to the higher atomic number of S and, thus, a larger number of electrons, highlighting the potential to develop novel scintillating SIC materials.[130−132]

Using high-temperature radioluminescence measurements, we observed thermal quenching of the $[Cs_6Cl]NaGa_6S_{12}:Mn^{2+}$ scintillation (Figure 10b and Figure S52), and emission was completely quenched at temperatures exceeding ~100 °C. The intensity of the 610 nm peak as a function of temperature was fit using a Mott−Seitz model for thermal quenching (Figure 10c and Figure S53).[98,133] This resulted in an estimate for the thermal quenching activation energy of 0.55 eV, which is consistent with the 0.45 eV measured for Mn^{2+} in Zn_2GeO_4.[98] Therefore, $[Cs_6Cl]NaGa_6S_{12}:Mn^{2+}$ materials are the first example of SIC compounds that demonstrated radiolumines-

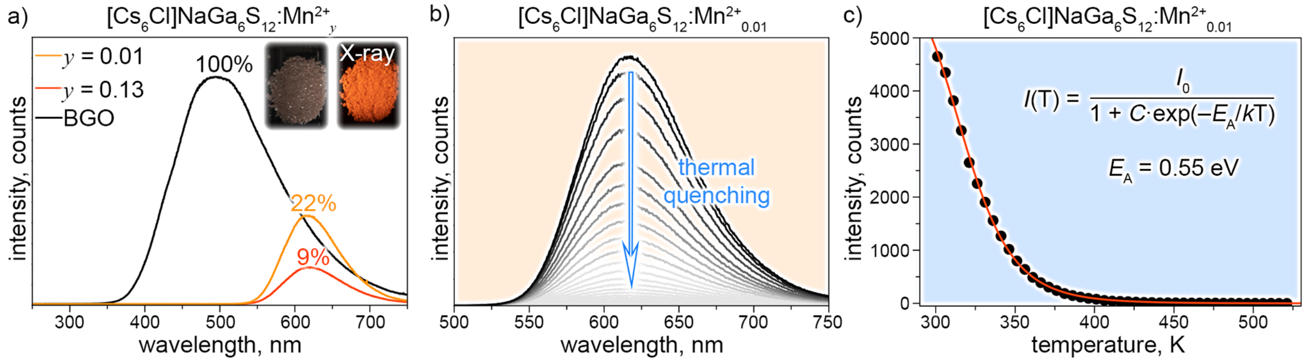

Figure 10. (a) Radioluminescence spectra of BGO (black), $[Cs_6Cl]NaGa_6S_{12}:Mn^{2+}{}_{0.01}$ (orange), and $[Cs_6Cl]NaGa_6S_{12}:Mn^{2+}{}_{0.13}$ (red). The percentage values correspond to relative scintillation intensity in comparison with the commercial scintillator, BGO. An insert of optical images demonstrates single crystals of $[Cs_6Cl]NaGa_6S_{12}:Mn^{2+}$: pristine and irradiated with X-ray. (b) Thermal quenching of $[Cs_6Cl]NaGa_6S_{12}:Mn^{2+}{}_{0.01}$ scintillation. (c) Radioluminescence peak intensity for $[Cs_6Cl]NaGa_6S_{12}:Mn^{2+}{}_{0.01}$ as a function of temperature. Peak intensity was fitted with a Mott−Seitz model, resulting in an E_A of 0.55 eV.

cent properties, suggesting the potential of SICs as scintillating materials.

CONCLUSIONS

Crystal growth in a halide/polychalcogenide flux resulted in the crystallization of a new family of salt-inclusion materials $[Cs_6X]AGa_6Q_{12}$. The $[Cs_6X]AGa_6Q_{12}$ structure consists of 0D $[Cs_6X]^{5+}$ fragment, 2D $[Ga_6Q_{12}]_n^{6n-}$ honeycomb layers, and *A* cations between the layers. These materials were shown to be kinetic products as demonstrated by testing their thermal stability, where increasing the reaction temperatures resulted in the dissociation of the structure into the thermodynamically more stable $(Cs/A)GaQ_2$ and $(A/Cs)X$. DFT calculations corroborated this decomposition path in the Cs−*X*−*A*−Ga−*Q* landscape. Although there are many combinations of covalent frameworks and salt-inclusion fragments, a fast stability screening of phase stability for SICs helped to identify more stable phases in the $[Cs_6X]AGa_6Q_{12}$ family.

The $[Cs_6X]AGa_6Q_{12}$ structure demonstrated the potential to undergo SC-SC ion-exchange reactions. Ion exchange in the melt affects only the salt-inclusion fragment *via* complete anion or partial cation exchange, e.g., $[Cs_6Cl]NaGa_6S_{12} \rightarrow [Cs_6F]NaGa_6S_{12}$ and $[Cs_6Br]NaGa_6Se_{12} \rightarrow [Cs_{6-x}Rb_xBr]NaGa_6Se_{12}$, respectively. In all cases, no exchange was observed for the non-salt-inclusion *A* site. It was demonstrated that ion-exchange reactions can be used to synthesize novel SICs compositions that do not form during flux crystal growth. Moreover, it was shown to be a viable approach for synthesizing fluoride-based SICs.

The Mn-doped $[Cs_6X]AGa_6Q_{12}$ structure exhibits photoluminescence ranging from orange (610 nm) to red (690 nm). Based on literature analysis and control experiments on $[Cs_6X]AGa_6Q_{12}:Mn^{2+}$ single crystals, these peaks were assigned to MnS_6 (610 nm) and MnS_4 (690 nm) fluorescent centers. However, additional structure characterization is needed to more precisely determine the local Mn coordination environments.[134] In general, it appears that SIC materials are a versatile platform for photophysics modulation due to diverse cation environments and abilities to activate luminesce using a variety of inorganic luminophores (Mn^{2+}, Ce^{3+}, and Eu^{2+}) as well as their combinations. Finally, $[Cs_6X]NaGa_6S_{12}:Mn^{2+}$ samples demonstrated scintillation properties, and the brightness of this novel scintillator was estimated to be 22% of BGO for a sample with the lowest Mn loading, $[Cs_6Cl]NaGa_6S_{12}:Mn^{2+}{}_{0.01}$. Future research may focus on developing new SIC materials for photoluminescence and radioluminescence applications and optimizing luminophore concentrations to enhance the SIC material's properties.

ASSOCIATED CONTENT

Supporting Information

The Supporting Information is available free of charge at https://pubs.acs.org/doi/10.1021/acs.chemmater.2c03592.

> Crystallographic tables, structure figures, PXRD patterns, EDS, UV−vis, photoluminescence, and scintillation spectra, DSC/TGA plot, and ICP-MS results (PDF)
>
> CIF file contains crystallographic information for $[Cs_6X]AGa_6Q_{12}$ (*A* = Na, K, and Rb; *X* = F, Cl, and Br; *Q* = S and Se) (CIF)

AUTHOR INFORMATION

Corresponding Author

Hans-Conrad zur Loye − *Department of Chemistry and Biochemistry, University of South Carolina, Columbia, South Carolina 29208, United States;* orcid.org/0000-0001-7351-9098; Email: zurloye@mailbox.sc.edu

Authors

Anna A. Berseneva − *Department of Chemistry and Biochemistry, University of South Carolina, Columbia, South Carolina 29208, United States*

Lakshani W. Masachchi − *Department of Chemistry and Biochemistry, University of South Carolina, Columbia, South Carolina 29208, United States*

Luiz G. Jacobsohn − *Department of Materials Science and Engineering, Clemson University, Clemson, South Carolina 29634, United States*

Complete contact information is available at: https://pubs.acs.org/10.1021/acs.chemmater.2c03592

Notes

The authors declare no competing financial interest.

ACKNOWLEDGMENTS

Research supported by the US Department of Energy, Office of Basic Energy Sciences, Division of Materials Sciences and Engineering under award DE-SC0018739. We thank Lijian He for the ICP-MS measurements. Radioluminescence measurements by L.G.J., who acknowledges support from the National Science Foundation under Grant No. 1653016.

REFERENCES

(1) Kanatzidis, M. G. Discovery-Synthesis, Design, and Prediction of Chalcogenide Phases. *Inorg. Chem.* **2017**, *56*, 3158−3173.

(2) Eggleton, B. J.; Luther-Davies, B.; Richardson, K. Chalcogenide Photonics. *Nat. Photonics* **2011**, *5*, 141−148.

(3) Mesbah, A.; Prakash, J.; Ibers, J. A. Overview of the Crystal Chemistry of the Actinide Chalcogenides: Incorporation of the Alkaline-Earth Elements. *Dalton Trans.* **2016**, *45*, 16067−16080.

(4) Tan, H.; Feng, Y.; Rui, X.; Yu, Y.; Huang, S. Metal Chalcogenides: Paving the Way for High-Performance Sodium/Potassium-Ion Batteries. *Small Methods* **2020**, *4*, No. 1900563.

(5) Nath, M.; Singh, H.; Saxena, A. Progress of Transition Metal Chalcogenides as Efficient Electrocatalysts for Energy Conversion. *Curr. Opin. Electrochem.* **2022**, *34*, No. 100993.

(6) Yin, J.; Jin, J.; Lin, H.; Yin, Z.; Li, J.; Lu, M.; Guo, L.; Xi, P.; Tang, Y.; Yan, C.-H. Optimized Metal Chalcogenides for Boosting Water Splitting. *Adv. Sci.* **2020**, *7*, No. 1903070.

(7) Zhang, J.; Bu, X.; Feng, P.; Wu, T. Metal Chalcogenide Supertetrahedral Clusters: Synthetic Control over Assembly, Dispersibility, and Their Functional Applications. *Acc. Chem. Res.* **2020**, *53*, 2261−2272.

(8) Soonmin, H.; Paulraj, I.; Kumar, M.; Sonker, R. K.; Nandi, P. *Chalcogenides - Preparation and Applications*; IntechOpen: 2022.

(9) Zhang, J.; Feng, P.; Bu, X.; Wu, T. Atomically Precise Metal Chalcogenide Supertetrahedral Clusters: Frameworks to Molecules, and Structure to Function. *Natl. Sci. Rev* **2022**, *9*, No. nwab076.

(10) Wang, G.; Luo, S.; Di, T.; Fu, Z.; Xu, G. Layered Organic Metal Chalcogenides (OMCs): From Bulk to Two-Dimensional Materials. *Angew. Chem., Int. Ed.* **2022**, *61*, No. e202203151.

(11) Tian, T.; Li, Z.; Wang, N.; Zhao, S.; Xu, J.; Lin, Z.; Mei, D. $Cs_2ZnSn_3S_8$: A Sulfide Compound Realizes a Large Birefringence by Modulating the Dimensional Structure. *Inorg. Chem.* **2021**, *60*, 9248−9253.

(12) Manos, M. J.; Kanatzidis, M. G. Metal Sulfide Ion Exchangers: Superior Sorbents for the Capture of Toxic and Nuclear Waste-Related Metal Ions. *Chem. Sci.* **2016**, *7*, 4804−4824.

(13) Pradel, A.; Ribes, M. Lithium Chalcogenide Conductive Glasses. *Mater. Chem. Phys.* **1989**, *23*, 121−142.

(14) Dai, H.; Xu, W.; Hu, Z.; Chen, Y.; Wei, X.; Yang, B.; Chen, Z.; Gu, J.; Yang, D.; Xie, F.; Zhang, W.; Guo, R.; Zhang, G.; Wei, W. Effective Approaches of Improving the Performance of Chalcogenide Solid Electrolytes for All-Solid-State Sodium-Ion Batteries. *Front. Energy Res.* **2020**, *8*, 97.

(15) Li, S.; Li, X.; Ren, Z.; Zhang, Q. Recent Progress towards High Performance of Tin Chalcogenide Thermoelectric Materials. *J. Mater. Chem. A* **2018**, *6*, 2432−2448.

(16) Han, C.; Sun, Q.; Li, Z.; Dou, S. X. Thermoelectric Enhancement of Different Kinds of Metal Chalcogenides. *Adv. Energy Mater.* **2016**, *6*, No. 1600498.

(17) Tesfaye, F. An Overview of Advanced Chalcogenide Thermoelectric Materials and Their Applications. *J. Elec. Res. Appl.* **2018**, *2*, 28−41.

(18) Berseneva, A. A.; Aziziha, M.; Schorne-Pinto, J.; Besmann, T. M.; zur Loye, H.-C. All-Inorganic Open-Framework Chalcogenides, $A_3Ga_5S_9{\cdot}xH_2O$ (A = Rb and Cs), Exhibiting Ultrafast Uranyl Remediation and Illustrating a Novel Post-Synthetic Preparation of Open-Framework Oxychalcogenides. *Chem. Mater.* **2022**, *34*, 8366−8378.

(19) Woods-Robinson, R.; Han, Y.; Zhang, H.; Ablekim, T.; Khan, I.; Persson, K. A.; Zakutayev, A. Wide Band Gap Chalcogenide Semiconductors. *Chem. Rev.* **2020**, *120*, 4007−4055.

(20) Tsujimoto, Y.; Juillerat, C. A.; Zhang, W.; Fujii, K.; Yashima, M.; Halasyamani, P. S.; zur Loye, H.-C. Function of Tetrahedral ZnS_3O Building Blocks in the Formation of $SrZn_2S_2O$: A Phase Matchable Polar Oxysulfide with a Large Second Harmonic Generation Response. *Chem. Mater.* **2018**, *30*, 6486−6493.

(21) Breton, L. S.; Klepov, V. V.; zur Loye, H.-C. Facile Oxide to Chalcogenide Conversion for Actinides Using the Boron-Chalcogen Mixture Method. *J. Am. Chem. Soc.* **2020**, *142*, 14365−14373.

(22) Berseneva, A. A.; Klepov, V. V.; Pal, K.; Seeley, K.; Koury, D.; Schaeperkoetter, J.; Wright, J. T.; Misture, S. T.; Kanatzidis, M. G.; Wolverton, C.; Gelis, A. V.; zur Loye, H.-C. Transuranium Sulfide *via* the Boron Chalcogen Mixture Method and Reversible Water Uptake in the $NaCuTS_3$ Family. *J. Am. Chem. Soc.* **2022**, *144*, 13773−13786.

(23) Breton, L. S.; Baumbach, R.; Tisdale, H. B.; zur Loye, H.-C. Structures and Magnetic Properties of $K_2Pd_4U_6S_{17}$, $K_2Pt_4U_6S_{17}$, $Rb_2Pt_4U_6S_{17}$, and $Cs_2Pt_4U_6S_{17}$ Synthesized Using the Boron-Chalcogen Mixture Method. *Inorg. Chem.* **2022**, *61*, 10502−10508.

(24) Jo, D. Y.; Kim, D.; Kim, J. H.; Chae, H.; Seo, H. J.; Do, Y. R.; Yang, H. Tunable White Fluorescent Copper Gallium Sulfide Quantum Dots Enabled by Mn Doping. *ACS Appl. Mater. Interfaces* **2016**, *8*, 12291−12297.

(25) Gu, C.; Xu, H. M.; Han, S. K.; Gao, M. R.; Yu, S. H. Soft Chemistry of Metastable Metal Chalcogenide Nanomaterials. *Chem. Soc. Rev.* **2021**, *50*, 6671−6683.

(26) Freitas, J. N.; Gonçalves, A. S.; Nogueira, A. F. A Comprehensive Review of the Application of Chalcogenide Nanoparticles in Polymer Solar Cells. *Nanoscale* **2014**, *6*, 6371−6397.

(27) Kyratsi, T.; Chung, D.-Y.; Choi, K.-S.; Dick, J. S.; Chen, W.; Uher, C.; Kanatzidis, M. Crystal Growth of Ternary and Quaternary Alkali Metal Bismuth Chalcogenides Using Bridgman Technique. *Mater. Res. Soc. Symp. Proc.* **2000**, *626*, Z8.8.

(28) Johnsen, S.; Liu, Z.; Peters, J. A.; Song, J.-H.; Peter, S. C.; Malliakas, C. D.; Cho, N. K.; Jin, H.; Freeman, A. J.; Wessels, B. W.; Kanatzidis, M. G. Thallium Chalcogenide-Based Wide-Band-Gap Semiconductors: $TlGaSe_2$ for Radiation Detectors. *Chem. Mater.* **2011**, *23*, 3120−3128.

(29) Laing, C. C.; Weiss, B. E.; Pal, K.; Quintero, M. A.; Xie, H.; Zhou, X.; Shen, J.; Chung, D. Y.; Wolverton, C.; Kanatzidis, M. G. $ACuZrQ_3$ (A = Rb, Cs; Q = S, Se, Te): Direct Bandgap Semiconductors and Metals with Ultralow Thermal Conductivity. *Chem. Mater.* **2022**, *34*, 8389−8402.

(30) Li, T.; Liu, Y. H.; Chitara, B.; Goldberger, J. E. Li Intercalation into 1D TiS_2(en) Chains. *J. Am. Chem. Soc.* **2014**, *136*, 2986−2989.

(31) Tulsky, E. G.; Long, J. R. Dimensional Reduction: A Practical Formalism for Manipulating Solid Structures. *Chem. Mater.* **2001**, *13*, 1149−1166.

(32) Morasse, R. A. L.; Li, T.; Baum, Z. J.; Goldberger, J. E. Rational Synthesis of Dimensionally Reduced TiS_2 Phases. *Chem. Mater.* **2014**, *26*, 4776−4780.

(33) Gamage, E. H.; Greenfield, J. T.; Unger, C.; Kamali, S.; Clark, J. K.; Harmer, C. P.; Luo, L.; Wang, J.; Shatruk, M.; Kovnir, K. Tuning Fe-Se Tetrahedral Frameworks by a Combination of $[Fe(en)_3]^{2+}$ Cations and Cl^- Anions. *Inorg. Chem.* **2020**, *59*, 13353−13363.

(34) Stahl, J.; Shlaen, E.; Singer, H.; Johrendt, D. Systematic Dimensional Reduction of the Layered β-FeSe Structure by Solvothermal Synthesis. *Dalton Trans.* **2018**, *47*, 3264−3271.

(35) Pak, C.; Kamali, S.; Pham, J.; Lee, K.; Greenfield, J. T.; Kovnir, K. Chemical Excision of Tetrahedral $FeSe_2$ Chains from the Superconductor FeSe: Synthesis, Crystal Structure, and Magnetism of $Fe_3Se_4(en)_2$. *J. Am. Chem. Soc.* **2013**, *135*, 19111−19114.

(36) Harmer, C. P.; Kamali, S.; Lebedev, O. I.; Lee, S. J.; Ribeiro, R. A.; Canfield, P. C.; Kovnir, K. Pseudo-Polymorphism in Layered FeS Intercalates: A Competition between Charged and Neutral Guest Species. *Chem. Mater.* **2022**, *34*, 5397−5408.

(37) Harmer, C. P.; Pak, C.; Greenfield, J. T.; Adeyemi, A. N.; Gamage, E. H.; Kovnir, K. Non-Innocent Intercalation of Diamines into Tetragonal FeS Superconductor. *ACS Appl. Energy Mater.* **2021**, *4*, 42−46.

(38) Pan, D.; Li, Y.; Han, Z.; Li, B.; Wang, C.; Yang, T.; Li, D.; Choi, C.; Zhang, Z. Organic−Inorganic Hybrid $(\beta\text{-}Fe_3Se_4)_4[Fe(teta)_{1.5}]$ (teta = triethylenetetramine) Nanoplates: Solution Synthesis and Magnetic Properties. *Chem. Mater.* **2018**, *30*, 8975−8982.

(39) Kuang, Q.; Men, X.; Shang, X.; Yang, B.; Zhou, Y.; Zhang, B.; Li, Z.; Li, D.; Zhang, Z. Magnetism of Tetragonal β-Fe_3Se_4 Nanoplates Controllably Synthesized by Thermal Decomposition of $(\beta\text{-}Fe_2Se_3)_4[Fe(tepa)]$ Hybrid. *Magnetism* **2022**, *2*, 31−44.

(40) Guo, M.; Lai, X.; Tan, X.; Xiao, M.; Wu, R.; Jian, J. Hydrazine Intercalated Iiron Sulfide $(N_2H_4)_{1\text{-}x}Fe_{2+\delta}S_2$: Synthesis and Characterization. *J. Solid State Chem.* **2021**, *303*, No. 122507.

(41) Pan, D.; Kuang, Q.; Tong, P.; Tong, W.; Fan, L.; Zhao, J.; Li, D.; Choi, C.; Zhang, Z. Self-Assembly of 1D $FeSe_2$ Chains and $Fe(dien)_2$ Complexes for Ferrimagnetic Inorganic-Organic Hybrid Cuboids. *J. Magn. Magn. Mater.* **2022**, *542*, No. 168585.

(42) Jin, S.; Fan, X.; Wu, X.; Sun, R.; Wu, H.; Huang, Q.; Shi, C.; Xi, X.; Li, Z.; Chen, X. High-T_c Superconducting Phases in Organic Molecular Intercalated Iron Selenides: Synthesis and Crystal Structures. *Chem. Commun.* **2017**, *53*, 9729−9732.

(43) Greenfield, J. T.; Pak, C.; Kamali, S.; Lee, K.; Kovnir, K. Control over Connectivity and Magnetism of Tetrahedral $FeSe_2$ Chains through Coordination Fe-amine Complexes. *Chem. Commun.* **2015**, *51*, 5355−5358.

(44) Yue, C.-Y.; Lei, X.-W.; Yin, L.; Zhai, X.-R.; Ba, Z.-R.; Niu, Y.-Q.; Li, Y.-P. $[Mn(dien)_2]MnSnS_4$, $[Mn(1,2\text{-}dap)]_2Sn_2S_6$ and $[Mn(en)_2]$-$MnGeS_4$: from 1D Anionic and Neutral Chains to 3D Neutral Frameworks. *CrystEngComm* **2015**, *17*, 814−823.

(45) McCarthy, C. L.; Brutchey, R. L. Solution Processing of Chalcogenide Materials Using Thiol-Amine "Alkahest" Solvent Systems. *Chem. Commun.* **2017**, *53*, 4888−4902.

(46) Yue, Q. G.; Wei, W. B.; Chen, H.; Wu, X. T.; Lin, H.; Zhu, Q. L. Salt-Inclusion Chalcogenides: an Emerging Class of IR Nonlinear Optical Materials. *Dalton Trans.* **2020**, *49*, 14338−14343.

(47) Choudhury, A.; Dorhout, P. K. Destruction of Noncentrosymmetry through Chalcogenide Salt Inclusion. *Inorg. Chem.* **2006**, *45*, 5245−5247.

(48) West, J. P.; Hwu, S.-J. Noncentrosymmetric Salt Inclusion Oxides: Role of Salt Lattices and Counter Ions in Bulk Polarity. *J. Solid State Chem.* **2012**, *195*, 101−107.

(49) Liu, B. W.; Jiang, X. M.; Li, B. X.; Zeng, H. Y.; Guo, G. C. $Li[LiCs_2\,Cl][Ga_3\,S_6\,]$: a Nanoporous Framework of GaS_4 Tetrahedra

with Excellent Nonlinear Optical Performance. *Angew. Chem., Int. Ed.* **2020**, *59*, 4856−4859.

(50) Liu, B. W.; Jiang, X. M.; Zeng, H. Y.; Guo, G. C. $[ABa_2Cl][Ga_4S_8]$ (A = Rb, Cs): Wide-Spectrum Nonlinear Optical Materials Obtained by Polycation-Substitution-Induced Nonlinear Optical (NLO)-Functional Motif Ordering. *J. Am. Chem. Soc.* **2020**, *142*, 10641−10645.

(51) Liu, B. W.; Zeng, H. Y.; Jiang, X. M.; Wang, G. E.; Li, S. F.; Xu, L.; Guo, G. C. $[A_3X][Ga_3PS_8]$ (A = K, Rb; X = Cl, Br): Promising IR Non-Linear Optical Materials Exhibiting Concurrently Strong Second-Harmonic Generation and High Laser Induced Damage Thresholds. *Chem. Sci.* **2016**, *7*, 6273−6277.

(52) Liu, B.-W.; Zeng, H.-Y.; Jiang, X.-M.; Guo, G.-C. Phase Matching Achieved by Bandgap Widening in Infrared Nonlinear Optical Materials $[ABa_3Cl_2][Ga_5S_{10}]$ (A= K, Rb, and Cs). *CCS Chem.* **2021**, *3*, 964−973.

(53) Chen, H.; Li, Y.-Y.; Li, B.; Liu, P.-F.; Lin, H.; Zhu, Q.-L.; Wu, X.-T. Salt-Inclusion Chalcogenide $[Ba_4Cl_2][ZnGa_4S_{10}]$: Rational Design of an IR Nonlinear Optical Material with Superior Comprehensive Performance Derived from $AgGaS_2$. *Chem. Mater.* **2020**, *32*, 8012−8019.

(54) Yu, P.; Zhou, L. J.; Chen, L. Noncentrosymmetric Inorganic Open-Framework Chalcohalides with Strong Middle IR SHG and Red Emission: $Ba_3AGa_5Se_{10}Cl_2$ (A = Cs, Rb, K). *J. Am. Chem. Soc.* **2012**, *134*, 2227−2235.

(55) Song, Y.; Cui, S.; Qian, Z.; Yu, H.; Hu, Z.; Wang, J.; Wu, Y.; Wu, H. $[ASr_4Cl][Ge_3S_{10}]$ (A = Na, K) and $[KBa_4Cl][Ge_3S_{10}]$: New Salt-Inclusion Infrared Nonlinear Optical Crystals with Zero-Dimensional $[Ge_3S_9]$ Clusters. *Inorg. Chem. Front.* **2022**, *9*, 5932−5940.

(56) Li, Y.-Y.; Liu, P.-F.; Hu, L.; Chen, L.; Lin, H.; Zhou, L.-J.; Wu, L.-M. Strong IR NLO Material $Ba_4MGa_4Se_{10}Cl_2$: Highly Improved Laser Damage Threshold *via* Dual Ion Substitution Synergy. *Adv. Opt. Mater.* **2015**, *3*, 957−966.

(57) Li, Y.-Y.; Liu, P.-F.; Lin, H.; Wang, M.-T.; Chen, L. The Effect of Indium Substitution on the Structure and NLO Properties of $Ba_6Cs_2Ga_{10}Se_{20}Cl_4$. *Inorg. Chem. Front.* **2016**, *3*, 952−958.

(58) Feng, K.; Kang, L.; Lin, Z.; Yao, J.; Wu, Y. Noncentrosymmetric Chalcohalide $NaBa_4Ge_3S_{10}Cl$ with Large Band Gap and IR NLO Response. *J. Mater. Chem. C* **2014**, *2*, 4590−4596.

(59) Liu, P. F.; Li, Y. Y.; Zheng, Y. J.; Yu, J. S.; Duan, R. H.; Chen, H.; Lin, H.; Chen, L.; Wu, L. M. Tailored Synthesis of Nonlinear Optical Quaternary Chalcohalides: $Ba_4Ge_3S_9Cl_2$, $Ba_4Si_3Se_9Cl_2$ and $Ba_4Ge_3Se_9Cl_2$. *Dalton Trans.* **2017**, *46*, 2715−2721.

(60) Xing, W.; Wang, N.; Iyer, A. K.; Yin, W.; Lin, Z.; Yao, J.; Kang, B.; Mar, A. Evaluation of Nonlinear Optical Properties of Quaternary Chalcogenide Halides $Ba_4Si_3Se_9Br_2$ and $Ba_4Ge_3Se_9Br_2$. *J. Alloys Compd.* **2020**, *846*, No. 156398.

(61) Guo, S. P.; Chi, Y.; Liu, B. W.; Guo, G. C. Synthesis, Crystal Structure and Second-Order Nonlinear Optical Property of a Novel Pentanary Selenide $(K_3I)[InB_{12}(InSe_4)_3]$. *Dalton Trans.* **2016**, *45*, 10459−10465.

(62) Han, S. S.; Yao, W. D.; Yu, S. X.; Sun, Y.; Gong, A.; Guo, S. P. A Series of Pentanary Salt-Inclusion Chalcogenoborates Containing a $B_{12}Q_{12}$ (Q = S, Se) Cluster Exhibiting a Kleinman-Forbidden Frequency-Doubling Effect. *Inorg. Chem.* **2021**, *60*, 3375−3383.

(63) Liu, H.; Song, Z.; Wu, H.; Hu, Z.; Wang, J.; Wu, Y.; Yu, H. $[Ba_2F_2][Ge_2O_3S_2]$: An Unprecedented Heteroanionic Infrared Nonlinear Optical Material Containing Three Typical Anions. *ACS Mater. Lett.* **2022**, *4*, 1593−1598.

(64) Chen, H.; Liu, P. F.; Lin, H.; Wu, X. T. A New Type of Novel Salt-Inclusion Chalcogenide with Ultralow Thermal Conductivity. *Chem. Commun.* **2020**, *56*, 15149−15152.

(65) Kabbour, H.; Cario, L.; Danot, M.; Meerschaut, A. Design of a New Family of Inorganic Compounds $Ae_2F_2SnX_3$ (Ae = Sr, Ba; X = S, Se) Using Rock Salt and Fluorite 2D Building Blocks. *Inorg. Chem.* **2006**, *45*, 917−922.

(66) Kabbour, H.; Cario, L.; Jobic, S.; Corraze, B. p-type Transparent Conductors $Sr_{1-x}Na_xFCuS$ and $SrF_{1-x}O_xCuS$: Design, Synthesis and Physical Properties. *J. Mater. Chem.* **2006**, *16*, 4165−4169.

(67) Kabbour, H.; Cario, L.; Boucher, F. Rational Design of New Inorganic Compounds with the ZrSiCuAs Structure Type Using 2D Building Blocks. *J. Mater. Chem.* **2005**, *15*, 3525.

(68) Lei, H.; Wang, K.; Abeykoon, M.; Bozin, E. S.; Petrovic, C. New Layered Fluorosulfide $SrFBiS_2$. *Inorg. Chem.* **2013**, *52*, 10685−10689.

(69) Liu, Y.; Zhang, S. B.; Li, L. J.; Lu, W. J.; Zhao, B. C.; Tong, P.; Song, W. H.; Lin, S.; Huang, Y. N.; Huang, Z. H.; Tan, S. G.; Sun, Y. P. Synthesis, Structure and Properties of the New Layered Manganese Oxyselenide $Sr_2F_2Mn_2Se_2O$. *J. Alloys Compd.* **2013**, *580*, 211−216.

(70) Sturza, M.; Allred, J. M.; Malliakas, C. D.; Bugaris, D. E.; Han, F.; Chung, D. Y.; Kanatzidis, M. G. Tuning the Magnetic Properties of New Layered Iron Chalcogenides $(BaF)_2Fe_{2-x}Q_3$ (Q = S, Se) by Changing the Defect Concentration on the Iron Sublattice. *Chem. Mater.* **2015**, *27*, 3280−3290.

(71) Higashinaka, R.; Endo, H.; Kajitani, J.; Matsuda, T. D.; Aoki, Y. Single Crystal Growth and Physical Properties of BiS_2-Layered Compound $Eu_3Bi_2S_4F_4$. *Phys. B* **2018**, *536*, 824−826.

(72) Luo, Z. Z.; Lin, C. S.; Cheng, W. D.; Li, Y. B.; Zhang, H.; Zhang, W. L.; He, Z. Z. Syntheses and Characterizations of Compounds $Ba_4F_4XGa_2S_6$ (X = Cr, Mn, Fe) and $Ba_4F_4MnIn_2S_6$ with 2D Layered Structures. *Dalton Trans.* **2013**, *42*, 9938−9945.

(73) Jha, R.; Tiwari, B.; Awana, V. P. S. Appearance of Bulk Superconductivity under Hydrostatic Pressure in $Sr_{0.5}RE_{0.5}FBiS_2$ (RE = Ce, Nd, Pr, and Sm) Compounds. *J. Appl. Phys.* **2015**, *117*, No. 013901.

(74) Lin, H.; Chen, H.; Lin, Z. X.; Zhao, H. J.; Liu, P. F.; Yu, J. S.; Chen, L. $(Cs_6Cl)_6Cs_3[Ga_{53}Se_{96}]$: A Unique Long Period-Stacking Structure of Layers Made from Ga_2Se_6 Dimers *via* Cis or Trans Intralayer Linking. *Inorg. Chem.* **2016**, *55*, 1014−1016.

(75) Wang, R.; Zhang, X.; Huang, F. $[Cs_6Cl][Ga_5GeQ_{12}]$ (Q = S, Se): Two Novel Porous Layered Chalcohalides Exhibiting Two-Band Emission and Ion Exchange Properties. *Sci. China: Chem.* **2022**, *65*, 1903−1910.

(76) Krause, L.; Herbst-Irmer, R.; Sheldrick, G. M.; Stalke, D. Comparison of Silver and Molybdenum Microfocus X-ray Sources for Single-Crystal Structure Determination. *J. Appl. Crystallogr.* **2015**, *48*, 3−10.

(77) Bruker (2012). *SAINT*; Bruker AXS Inc.: Madison, Wisconsin, USA.

(78) Dolomanov, O. V.; Bourhis, L. J.; Gildea, R. J.; Howard, J. A. K.; Puschmann, H. *OLEX2*: a Complete Structure Solution, Refinement and Analysis Program. *J. Appl. Crystallogr.* **2009**, *42*, 339−341.

(79) Sheldrick, G. M. Crystal Structure Refinement with SHELXL. *Acta Cryst.* **2015**, *71*, 3−8.

(80) Kresse, G.; Furthmüller, J. Efficiency of *ab-initio* Total Energy Calculations for Metals and Semiconductors Using a Llane-Wave Basis Set. *Comput. Mater. Sci.* **1996**, *6*, 15−50.

(81) Kresse, G.; Furthmüller, J. Efficient Iterative Schemes for *ab initio* Total-Energy Calculations Using a Plane-Wave Basis Set. *Phys. Rev. B: Condens. Matter Mater. Phys.* **1996**, *54*, 11169−11186.

(82) Kresse, G.; Joubert, D. From Ultrasoft Pseudopotentials to the Projector Augmented-wave Method. *Phys. Rev. B: Condens. Matter Mater. Phys.* **1999**, *59*, 1758−1775.

(83) Perdew, J. P.; Burke, K.; Ernzerhof, M. Generalized Gradient Approximation Made Simple. *Phys. Rev. Lett.* **1996**, *77*, 3865−3868.

(84) Kirklin, S.; Saal, J. E.; Meredig, B.; Thompson, A.; Doak, J. W.; Aykol, M.; Rühl, S.; Wolverton, C. The Open Quantum Materials Database (OQMD): Assessing the Accuracy of DFT Formation Energies. *npj Comput. Mater.* **2015**, *1*, 15010.

(85) Saal, J. E.; Kirklin, S.; Aykol, M.; Meredig, B.; Wolverton, C. Materials Design and Discovery with High-Throughput Density Functional Theory: The Open Quantum Materials Database (OQMD). *JOM* **2013**, *65*, 1501−1509.

(86) Bergstrom, F. W. The Polysulfides and Polyselenides of Lithium, Sodium and Potassium. *J. Am. Chem. Soc.* **1926**, *48*, 146−151.

(87) Klepov, V. V.; Juillerat, C. A.; Pace, K. A.; Morrison, G.; zur Loye, H.-C. "Soft" Alkali Bromide and Iodide Fluxes for Crystal Growth. *Front. Chem* **2020**, *8*, 518.

(88) Huang-Fu, S. X.; Shen, J. N.; Lin, H.; Chen, L.; Wu, L. M. Supercubooctahedron $(Cs_6Cl)_2Cs_5[Ga_{15}Ge_9Se_{48}]$ Exhibiting Both Cation and Anion Exchange. *Chem. - Eur. J.* **2015**, *21*, 9809−9815.

(89) Gao, H.; Chen, R.; Zhang, K.; Abudurusuli, A.; Lai, K.; Li, J. Synthesis, Characterization and Theoretical Investigation of a New Chalcohalide, $Ba_4GaS_4F_3$. *Dalton Trans.* **2021**, *50*, 6315−6320.

(90) Feng, K.; Yin, W.; Lin, Z.; Yao, J.; Wu, Y. Five New Chalcohalides, Ba_3GaS_4X (X = Cl, Br), Ba_3MSe_4Cl (M = Ga, In), and $Ba_7In_2Se_6F_8$: Syntheses, Crystal Structures, and Optical Properties. *Inorg. Chem.* **2013**, *52*, 11503−11508.

(91) Li, M. Y.; Zhang, Y. X.; Lin, H.; Ma, Z.; Wu, X. T.; Zhu, Q. L. Combined Experimental and Theoretical Investigations of Ba_3GaS_4I: Interesting Structural Transformation Originated from Halogen Substitution. *Dalton Trans.* **2019**, *48*, 17588−17593.

(92) Li, X.; Liang, F.; Liu, T.; Li, H. Na_2GaS_2Cl: a New Sodium-Rich Chalcohalide with Two-Dimensional $[GaS_2]_\infty$ Layers and Wide Interlayer Space. *Dalton Trans.* **2021**, *50*, 11167−11172.

(93) Pei, S.-M.; Liu, B.-W.; Jiang, X.-M.; Zou, Y.-Q.; Chen, W.-F.; Yan, Q.-N.; Guo, G.-C. Superior Infrared Nonlinear Optical Performance Achieved by Synergetic Functional Motif and Vacancy Site Modulations. *Chem. Mater.* **2021**, *33*, 8831−8837.

(94) Guo, S. P.; Guo, G. C.; Wang, M. S.; Zou, J. P.; Zeng, H. Y.; Cai, L. Z.; Huang, J. S. A Facile Approach to Hexanary Chalcogenoborate Featuring a 3-D Chiral Honeycomb-Like Open-Framework Constructed from Rare-Earth Consolidating Thiogallate-closo-Dodecaborate. *Chem. Commun.* **2009**, 4366−4368.

(95) Yin, W.; Iyer, A. K.; Xing, W.; Kang, B.; Mar, A. Quaternary Chalcogenide Halides Ba_3GaSe_4Br and Ba_3InSe_4Br. *J. Solid State Chem.* **2020**, *284*, No. 121189.

(96) Sangster, J.; Pelton, A. D. The Na-S (Sodium-Sulfur) System. *J. Phase Equilib.* **1997**, *18*, 89−96.

(97) Kabbour, H.; Cario, L. $Ba_2F_2Fe^{2+}{}_{0.5}Fe^{3+}S_3$: a Two-Dimensional Inhomogeneous Mixed Valence Iron Compound. *Inorg. Chem.* **2008**, *47*, 1648−1652.

(98) Chi, F.; Wei, X.; Jiang, B.; Chen, Y.; Duan, C.; Yin, M. Luminescence Properties and the Thermal Quenching Mechanism of Mn^{2+}-doped Zn_2GeO_4 Long Persistent Phosphors. *Dalton Trans.* **2018**, *47*, 1303−1311.

(99) Lin, J.; Zhang, Q.; Wang, L.; Liu, X.; Yan, W.; Wu, T.; Bu, X.; Feng, P. Atomically Precise Doping of Monomanganese Ion into Coreless Supertetrahedral Chalcogenide Nanocluster Inducing Unusual Red Shift in Mn^{2+} Emission. *J. Am. Chem. Soc.* **2014**, *136*, 4769−4779.

(100) Suzuki, A.; Hidaka, C.; Takizawa, T.; Nomura, S. Analysis of the Enhancing Effect of Rare Earth Ion Co-Doping on the Red Emission of $CaGa_2S_4$:Mn^{2+}in View of Its Decay Time. *Jpn. J. Appl. Phys.* **2011**, *50*, No. 05FG03.

(101) Collins, B. T.; Ling, M. Synthesis and Cathodoluminescence of Orange-Yellow- to Red-Emitting $Ca_{1-x}Mg_xS$:Mn Phosphors. *J. Electrochem. Soc.* **1993**, *140*, 1752−1755.

(102) Ihanus, J.; Hänninen, T.; Hatanpää, T.; Ritala, M.; Leskelä, M. Electroluminescent SrS and BaS Thin Films Deposited by ALD Using Cyclopentadienyl Precursors. *J. Electrochem. Soc.* **2004**, *151*, H221.

(103) Collins, B. T.; Ling, M. Synthesis and Cathodoluminescent Performance of Green-Emitting SrS:Mn Phosphors. *J. Electrochem. Soc.* **1996**, *143*, 2328−2331.

(104) Yamashita, N.; Shuji, M.; Nakamura, K. Influence of Paired Mn^{2+} Centers on the Luminescence Spectra of CaS:Mn^2. *Jpn. J. Appl. Phys.* **1990**, *29*, 1729−1731.

(105) Jiang, T.; Ma, W.; Zhang, H.; Tian, Y.; Lin, G.; Xiao, W.; Yu, X.; Qiu, J.; Xu, X.; Yang, Y. (. M.).; Ju, D. Highly Efficient and Tunable Emission of Lead-Free Manganese Halides toward White Light-Emitting Diode and X-Ray Scintillation Applications. *Adv. Funct. Mater.* **2021**, *31*, No. 2009973.

(106) Wang, H.; Wang, W.; Hu, D.; Luo, M.; Xue, C.; Li, D.; Wu, T. Hybrid Assembly of Different-Sized Supertetrahedral Clusters into a Unique Non-Interpenetrated Mn-In-S Open Framework with Large Cavity. *Inorg. Chem.* **2018**, *57*, 6710−6715.

(107) Su, F. H.; Fang, Z. L.; Ma, B. S.; Ding, K.; Li, G. H.; Chen, W. Pressure Dependence of Mn^{2+} Luminescence in Differently Sized ZnS:Mn Nanoparticles. *J. Phys. Chem. B* **2003**, *107*, 6991−6996.

(108) Lee, J.-S.; Won, Y.-H.; Kim, H.-N.; Kim, C.-D.; Kim, W.-T. Photoluminescence of Ga_2S_3 and Ga_2S_3: Mn Single Crystals. *Solid State Commun.* **1996**, *97*, 1101−1104.

(109) Wang, C.; Wang, Z.; Li, P.; Cheng, J.; Li, Z.; Tian, M.; Sun, Y.; Yang, Z. Relationships between Luminescence Properties and Polyhedron Distortion in $Ca_{9-x-y-z}Mg_xSr_yBa_zCe(PO_4)_7$:$Eu^{2+}$,$Mn^{2+}$. *J. Mater. Chem. C* **2017**, *5*, 10839−10846.

(110) Liang, S.; Dang, P.; Li, G.; Molokeev, M. S.; Wei, Y.; Wei, Y.; Lian, H.; Shang, M.; Al Kheraif, A. A.; Lin, J. Controllable Two-Dimensional Luminescence Tuning in Eu^{2+},Mn^{2+} Doped $(Ca,Sr)_9Sc(PO_4)_7$ Based on Crystal Field Regulation and Energy Transfer. *J. Mater. Chem. C* **2018**, *6*, 6714−6725.

(111) Miao, S.; Xia, Z.; Molokeev, M. S.; Chen, M.; Zhang, J.; Liu, Q. Effect of Al/Si Substitution on the Structure and Luminescence Properties of $CaSrSiO_4$:Ce^{3+} Phosphors: Analysis Based on the Polyhedra Distortion. *J. Mater. Chem. C* **2015**, *3*, 4616−4622.

(112) Zhu, Y.; Liang, Y.; Liu, S.; Li, H.; Chen, J.; Lei, W. A Strategy for Realizing Tunable Luminescence and Full-Color Emission in $Sr_3Gd_2(Si_3O_9)_2$:Eu Phosphors by Introducing Dual Functional Mn^{2+}. *Inorg. Chem. Front.* **2018**, *5*, 2527−2539.

(113) Askerov, I.; Okuducu, Ş. Electron Spin Resonance and Luminescence in $Ga_{2-x}Eu_xS_3$ Single Crystals. *J. Phys. Chem. Solids* **2003**, *64*, 1929−1933.

(114) Klepov, V. V.; Kocevski, V.; Besmann, T. M.; zur Loye, H.-C. Dimensional Reduction upon Calcium Incorporation in $Cs_{0.3}(Ca_{0.3}Ln_{0.7})PS_4$ and $Cs_{0.5}(Ca_{0.5}Ln_{0.5})PS_4$. *CrystEngComm* **2021**, *23*, 831−840.

(115) Breton, L. S.; Smith, M. D.; zur Loye, H.-C. Trends in Rare Earth Thiophosphate Syntheses: $Rb_3Ln(PS_4)_2$ (Ln = La, Ce, Pr), $Rb_{3-x}Na_xLn(PS_4)_2$ (Ln = Ce, Pr; x = 0.50, 0.55), and $RbEuPS_4$ Obtained by Molten Flux Crystal Growth. *CrystEngComm* **2021**, *23*, 5241−5248.

(116) Kutahyali Aslani, C.; Breton, L. S.; Klepov, V. V.; zur Loye, H.-C. A Series of $Rb_4Ln_2(P_2S_6)(PS_4)_2$ (Ln = La, Ce, Pr, Nd, Sm, Gd) Rare Earth Thiophosphates with Two Distinct Thiophosphate Units $[P^VS_4]^{3-}$ and $[P^{IV}{}_2S_6]^4$. *Dalton Trans.* **2021**, *50*, 1683−1689.

(117) Yan, Q.; Liu, Y.; Wang, W.; Chen, G. Luminescence Behaviors of the Eu^{2+} Ions in the GeS_2-Ga_2S_3-CsCl Chalcohalide Glasses. *J. Non-Cryst. Solids* **2011**, *357*, 2472−2474.

(118) López-Lugo, V. H.; Rivera-Medina, M. J.; Alonso-Huitrón, J. C. Quantitative Assessing of Crystal Field, Nephelauxetic, and Stokes Shift Effects on the Blue Luminescence of Eu^{2+} Ions Incorporated in ZnS Films. *Mater. Res. Express* **2021**, *8*, No. 036406.

(119) Urmanov, B. D.; Leanenia, M. S.; Yablonskii, G. P.; Taghiyev, O. B.; Taghiyev, K. O.; Kazimova, F. A.; Ibragimova, T. S. Photoluminescence of $Ca_4Ga_2S_7$:Eu^{2+} in Wide Excitation Intensity and Temperature Range. *Mod. Phys. Lett. B* **2021**, *35*, No. 2150392.

(120) Qu, M.; Pang, Z.; Li, T.; Liu, Q.; Yang, Y.; Zhang, X. Wide-Band Blue-Emitting in Ce^{3+} Doped $Ca_2YZr_2Al_3O_{12}$ Garnet-Type Phosphor Designed *via* Local Structural Lattice Distortion and Synthesized in Nonreducing Atmosphere. *Ceram. Int.* **2023**, *49*, 792−800.

(121) Zhuo, Y.; Hariyani, S.; Zhong, J.; Brgoch, J. Creating a Green-Emitting Phosphor through Selective Rare-Earth Site Preference in $NaBaB_9O_{15}$:Eu^{2+}. *Chem. Mater.* **2021**, *33*, 3304−3311.

(122) Park, J.; Lee, J.-W.; Singh, S. P.; Kim, M.; Lee, B. D.; Park, W. B.; Sohn, K.-S. A Novel Sulfide Phosphor, $BaNaAlS_3$:Eu^{2+} Discovered *via* Particle Swarm Optimization. *J. Alloys Compd.* **2022**, *922*, No. 166187.

(123) Montanarella, F.; McCall, K. M.; Sakhatskyi, K.; Yakunin, S.; Trtik, P.; Bernasconi, C.; Cherniukh, I.; Mannes, D.; Bodnarchuk, M. I.; Strobl, M.; Walfort, B.; Kovalenko, M. V. Highly Concentrated, Zwitterionic Ligand-Capped Mn^{2+}:$CsPb(Br_xCl_{1-x})_3$ Nanocrystals as Bright Scintillators for Fast Neutron Imaging. *ACS Energy Lett.* **2021**, *6*, 4365−4373.

(124) Kato, T.; Okada, G.; Yanagida, T. Optical, Scintillation and Dosimeter Properties of MgO Transparent Ceramic Doped with Mn^{2+}. *J. Ceram. Soc. Jpn.* **2016**, *124*, 559−563.

(125) Chen, S.; Gong, Y.; Huang, W.; Wen, Z.; Li, L.; Ashraf, G. A.; Lei, L.; Cao, J.; Guo, H. Intense Broadband Radioluminescence from an Mn^{2+}-Doped Aluminoborate Glass Scintillator. *J. Mater. Chem. C* **2022**, *10*, 10382−10388.
(126) Li, X.; Chen, J.; Yang, D.; Chen, X.; Geng, D.; Jiang, L.; Wu, Y.; Meng, C.; Zeng, H. Mn^{2+} Induced Significant Improvement and Robust Stability of Radioluminescence in $Cs_3Cu_2I_5$ for High-Performance Nuclear Battery. *Nat. Commun.* **2021**, *12*, 3879.
(127) Tang, G.; Hua, Z.; Wei, Q.; Qin, L.; Huang, Y.; Cai, P.; Bai, G.; Zhou, Z.; Zhou, G.; Ren, J.; Sui, Z.; Qian, S.; Wang, Z.White-Light Emission and Red Scintillation from Mn^{2+} Ions Single-Doped Aluminum-Silicate Glasses. *SSRN Electronic Journal* 4243325.
(128) Galleani, G.; Lodi, T. A.; Mastelaro, V. R.; Jacobsohn, L. G.; de Camargo, A. S. S. Photoluminescence and X-ray Induced Scintillation in Gd^{3+}-Modified Fluorophosphate Glasses Doped with Ce^{3+}. *Opt. Mater.* **2022**, *133*, No. 112934.
(129) Pinto, I. C.; Galleani, G.; Jacobsohn, L. G.; Ledemi, Y.; Messaddeq, Y.; de Camargo, A. S. S. Fluorophosphate Glasses Doped with Eu^{3+} and Dy^{3+} for X-ray Radiography. *J. Alloys Compd.* **2021**, *863*, No. 158382.
(130) He, Y.; Hadar, I.; De Siena, M. C.; Klepov, V. V.; Pan, L.; Chung, D. Y.; Kanatzidis, M. G. Sensitivity and Detection Limit of Spectroscopic-Grade Perovskite $CsPbBr_3$ Crystal for Hard X-Ray Detection. *Adv. Funct. Mater.* **2022**, *32*, No. 2112925.
(131) Weber, M. J. Inorganic Scintillators: Today and Tomorrow. *J. Lumin.* **2002**, *100*, 35−45.
(132) Kumar, V.; Luo, Z. A Review on X-ray Excited Emission Decay Dynamics in Inorganic Scintillator Materials. *Photonics* **2021**, *8*, 71.
(133) Pagonis, V.; Ankjærgaard, C.; Murray, A. S.; Jain, M.; Chen, R.; Lawless, J.; Greilich, S. Modelling the Thermal Quenching Mechanism in Quartz Based on Time-Resolved Optically Stimulated Luminescence. *J. Lumin.* **2010**, *130*, 902−909.
(134) Carone, D.; Klepov, V. V.; Misture, S. T.; Schaeperkoetter, J. C.; Jacobsohn, L. G.; Aziziha, M.; Schorne-Pinto, J.; Thomson, S. A. J.; Hines, A. T.; Besmann, T. M.; zur Loye, H.-C. Luminescence and Scintillation in the Niobium Doped Oxyfluoride $Rb_4Ge_5O_9F_6$:Nb. *Inorganics* **2022**, *10*, 83.

https://doi.org/10.1021/acs.chemmater.2c03592